

ABSTRACT

Title of dissertation: Chiral Quantum Optics
using Topological Photonics

Sabyasachi Barik
Doctor of Philosophy, 2020

Dissertation directed by: Professor Edo Waks and Professor Mohammad Hafezi
Department of Physics

Topological photonics has opened new avenues to designing photonic devices along with opening a plethora of applications. Recently, even though there have been many interesting studies in topological photonics in the classical domain, the quantum regime has remained largely unexplored. In this thesis, I will demonstrate a recently developed topological photonic crystal structure for interfacing a single quantum dot spin with a photon to realize light-matter interaction with topological photonic states. Developed on a thin slab of Gallium Arsenide(GaAs) membrane with electron beam lithography, such a device supports two robust counter-propagating edge states at the boundary of two distinct topological photonic crystals at near-IR wavelength. I will show the chiral coupling of circularly polarized lights emitted from a single Indium Arsenide(InAs) quantum dot under a strong magnetic field into these topological edge modes. Owing to the topological nature of these guided modes, I will demonstrate this photon routing to be robust against sharp corners along the waveguide. Additionally, taking it further into the cavity-QED

regime, we will build a topological photonic crystal resonator. This new type of resonator will be based on valley-Hall topological physics and sustain two counter-propagating resonator modes. Thanks to the robustness of the topological edge modes to sharp bends, the newly formed resonators can take various shapes, the simplest one being a triangular optical resonator. We will study the chiral coupling of such resonator modes with a single quantum dot emission. Moreover, we will show an intensity enhancement of a single dot emission when it resonantly couples with a cavity mode. This new topological photonic crystal platform paves paths for fault-tolerant complex photonic circuits, secure quantum computation, and exploring unconventional quantum states of light and chiral spin networks.

CHIRAL QUANTUM OPTICS USING TOPOLOGICAL
PHOTONICS

by

Sabyasachi Barik

Dissertation submitted to the Faculty of the Graduate School of the
University of Maryland, College Park in partial fulfillment
of the requirements for the degree of
Doctor of Philosophy
2020

Advisory Committee:
Professor Edo Waks, Chair/Advisor
Professor Mohammad Hafezi, Co-Advisor
Professor Thomas Murphy
Professor Trey Porto
Professor Rajarshi Roy
Professor John Cumings

© Copyright by
Sabyasachi Barik
2020

Dedicated to my loved ones

Acknowledgments

I owe my gratitude to all the people who have made this thesis possible and who have made my graduate experience one that I will cherish forever.

First and foremost, I'd like to thank my advisor, Professor Edo Waks, for giving me an invaluable opportunity to work on challenging and extremely interesting projects over the past six years. He has always made himself available for help and advice, and there has never been an occasion when I've knocked on his door and he hasn't given me time. It has been a pleasure to work with and learn from such an extraordinary individual.

I would also like to thank my co-advisor, Professor Mohammad Hafezi. Without his extraordinary theoretical ideas and computational expertise, this thesis would have been a distant dream. Thanks are due to Professor Thomas Murphy, Professor Trey Porto and Professor Rajarshi Roy for agreeing to serve on my thesis committee and for sparing their invaluable time reviewing the manuscript. A special thanks goes to Professor John Cumings for agreeing to be the dean's representative and helping me out tremendously at short notice.

I am indebted to Professor Thomas Murphy for all the insightful discussions. His clear perception, intellectual contributions and expertise in scientific writing and presentation have been immensely valuable.

My colleagues at the Quantum Nanophotonics group have enriched my graduate life in many ways and deserve a special mention. I would like to thank Dr. Hirokazu Miyake for being an excellent mentor in my first two years as a PhD stu-

dent. I learned so many experimental techniques by shadowing him in the lab and discussing with him. In particular, I would like to thank Dr. Tao Cai and Dr. Shuo Sun for sharing with me all of their hands-on experiences ranging from optical alignment to nano-fabrications. They helped me start off by guiding me through the lab and getting started on the compact optical setups along with help regarding simulations. I would also express my gratitude to Dr. Hamidreza Chalabi for being an excellent mentor and collaborator during my PhD research. I learned a lot of simulation techniques and honed my computational skills while working with him.

Thanks also go to my collaborators including Professor Glenn Solomon, Professor Thomas Murphy and Dr. Wade DeGottardi. None of my research work could be carried out without their sincere support. My interactions with Dr. Shahriar Aghaeimeibodi, Subhojit Dutta, Aziz Karasahin, Zhouchen Luo, Mustafa Atabey Büyükkaya, Chris Flower, Uday Saha and Harjot Singh have always been very fruitful. I would like to acknowledge my past and present lab mates for their support: Dr. Hyochul Kim, Dr. Chad Ropp, Dr. Shilpi Gupta, Dr. Kangmook Lim, Dr. Kaushik Roy Choudhury, Dr. Je-hyung Kim, Dr. Jose Algarin, Dr. Zhili Yang, Peng Zhou, Dr. Youngmin Martin Kim, Dr. Dima Farfurnik, Dr. Chang-Min Lee, Dr. Robert Pettit, Yu Shi, Chang-Mu Han, Sam Harper, Shantam Ravan, Yuqi Zhao and Xinyuan Zheng.

I am also grateful to members of Professor Mohammad Hafezi's group at JQI including Professor Elizabeth Goldschmidt and Dr. Sunil Mittal, who provided a cordial atmosphere in the lab. They were always available for any kind of help in setting up the experiments and discussing theory.

I acknowledge support from technicians in the UMD nanofabrication center: Tom Loughran, Mark Lecates, Jon Hummel, John Abrahams, and Wen-an Chiou. I thank them all for maintaining the equipment in good shape and always being there to help when necessary. I would also like to thank all the staff members in IREAP, past and present, Bryan Quinn, Don Schmadel, Thomas Weimar, Kathryn Tracey, Leslie Delabar, and Judi Cohn Gorski . Specially, Nolan's technical help is highly appreciated, as is the computer hardware support from Edward Condon, LaTeX and software help from Dorothea Brosius, purchasing help from Nancy Boone and travel related help from Taylor Prendergast.

I owe my deepest thanks to my family - my mother and father who have always stood by me and guided me through my career, and have pulled me through against impossible odds at times. Words cannot express the gratitude I owe them. A special thanks goes to my younger brother Biplab. His cheerful attitude always gave me that additional boost. I would also like to thank Sarthak, Subhojit, Tiffany, Aditya, Swarnav, Tamoghna who are like family members to me. My housemates at my place of residence have been a crucial factor in my finishing smoothly. I'd like to express my gratitude to Soubhik and Amit for their friendship and support.

I would like to acknowledge financial support from the Office of Naval Research (ONR), Air Force Office of Scientific Research (AFOSR), Sloan Foundation and the Physics Frontier Center (PFC) at the Joint Quantum Institute (JQI) for all the projects discussed herein.

It is impossible to remember all, and I apologize to those I've inadvertently left out.

Lastly, thank you all!

Table of Contents

Preface	ii
Acknowledgements	iii
Table of Contents	vii
List of Tables	x
List of Figures	xi
List of Abbreviations	xiii
List of Publications to Date	xiv
Chapter 1: Introduction	1
1.1 Brief Overview	1
1.2 Outline of Thesis	5
Chapter 2: Topological Edge States in Photonic Crystals	7
2.1 Review	7
2.2 Proposed structure	9
2.2.1 Honeycomb Lattice with Circular Holes	9
2.2.2 Honeycomb Lattice with Triangular Holes	11
2.3 Band structure for TE modes	13
2.3.1 Band Folding	15
2.3.2 Perturbation to the system parameters	15
2.3.3 Band inversion	16
2.4 Topological edge sates	16
2.4.1 Non-trivial topology	16
2.4.2 One-dimensional band structure	18
2.5 Unidirectional propagation	18
2.5.1 Helical nature of edge states	18
2.5.2 Topological confinement	18
2.6 Topological protection and robustness	20
2.7 Discussion	20

Chapter 3: Chiral coupling of a single photon inside a Topological Photonic Crystal Waveguide	22
3.1 Review	22
3.2 Fabricated structure	23
3.2.1 Device Design	23
3.2.2 SEM image	24
3.2.3 Band structures : FDTD results	26
3.3 Waveguiding via edge states	28
3.3.1 Transmission of the waveguide	28
3.3.2 Probing the guided modes at the interface	28
3.4 Observation of chiral coupling of a single emitter	29
3.4.1 Zeeman effect	29
3.4.2 Polarization of Quantum Dots Under Magnetic Field	29
3.4.3 Chiral coupling of quantum dot emission into the waveguide	30
3.5 Topological robustness	32
3.5.1 Waveguiding across a bend	32
3.5.2 Routing single photon	34
3.5.3 Robustness to disorder	34
3.6 Discussion	35
Chapter 4: Quantum optics with topological photonic crystal resonator	37
4.1 Review : Chiral quantum optics	37
4.2 Proposed Structure	39
4.2.1 Valley-Hall topological photonic crystal	39
4.2.2 Fabricated resonator structure	41
4.2.3 Simulation results	41
4.3 Observation of topological resonator modes	42
4.4 Observation of chiral coupling of an emitter inside topological resonator	44
4.4.1 Waveguide-Resonator Hybrid Device : FDTD results	44
4.4.2 Chiral coupling	46
4.4.3 Polarization-momentum locking	46
4.5 Intensity enhancement of a single emitter coupled to the resonator	48
4.6 Summary	50
Chapter 5: Conclusion and Outlook	51
Appendix A:	54
A.1 Honeycomb Lattice with a Six-Site Basis and Band Folding	54
A.2 Tight-Binding Description of the Dispersion	55
A.3 Topology and Edge States	62
A.4 Inversion of the Eigenstates	65
A.5 Polarization Pseudo-Spin of the Eigenstates	67
Appendix B:	69
B.1 Device Fabrication	69

B.2	Experimental Setup	71
B.3	Grating Calibration	72
B.4	Coupling Efficiency	73
Appendix C:		75
C.1	The polarization profile of a topological resonator	75
C.2	Sample fabrication	75
C.3	Measurements	77
C.4	The quality factor of resonator in hybrid structures	78
C.5	Resonator designs with Valley-Hall physics	79
Bibliography		81

List of Tables

B.1 Estimation of coupling efficiency	74
---	----

List of Figures

2.1	Band structure of a honeycomb lattice with circular holes	10
2.2	Schematic of our proposed honeycomb-lattice-like photonic crystal . .	12
2.3	Band structures show opening and closing of a band gap around the Dirac point as we perturb the lattice.	14
2.4	Schematic and band structure which gives rise to topological edge states.	17
2.5	Three-dimensional, vertically-confined topological edge states at optical frequencies in an all-dielectric material.	19
3.1	Design of honeycomb-like photonic crystal	24
3.2	Fabricated device and band structure	25
3.3	Transmission characteristics of the topological waveguide	27
3.4	Polarization of quantum dot emission in bulk under magnetic field . .	30
3.5	Chirality in a straight topological waveguide	31
3.6	Robust transport in two dimensions along a bend	33
3.7	Effect of defects on the transmission of edge modes	35
4.1	Valley-Hall topological photonic crystal resonator and FDTD simulation results	40
4.2	Topological waveguide-resonator system	43
4.3	Chiral waveguide-resonator-emitter coupling	45
4.4	Position dependent spin-momentum locking	47
4.5	Purcell enhancement of a quantum emitter coupled to a topological resonator	49
A.1	Correspondence between the two-site and six-site bases	56
A.2	Schematic of our lattice parameters and the labeling of the lattice sites for our tight-binding model	58
A.3	Physics of band inversion	66
A.4	Out-of-plane magnetic field and in-plane electric field polarization . .	68
B.1	Mask design for fabrication of triangles	70
B.2	Transmission data from left and right gratings	73
C.1	Simulated left/right circular polarization components of the electric field	76

C.2 Schematic of the experimental setup	77
C.3 Quality factor of cavity in hybrid structure	79
C.4 More resonator ideas	80

List of Abbreviations

QD	Quantum Dot
QED	quantum electrodynamics
qubit	quantum bit
PBS	Polarization Beam Splitter
InAs	Indium Arsenide
GaAs	Gallium Arsenide
InP	Indium Phosphide
FDTD	finite-difference time-domain
SPCM	Single Photon Counting Module
LED	Light Emitting Diode
HF	Hydro Flouric

List of Publications to Date

1. S Barik et al. “Chiral quantum optics using a topological resonator”, *Physical Review B* 101 (20), 205303 (2020)
2. H Chalabi, S Barik et al. ” Guiding and confining of light in a two-dimensional synthetic space using electric fields” *Optica* 7 (5), 506-513 (2020)
3. S Barik, M Hafezi, “Robust and compact waveguides”, *Nature Nanotechnology* 14 (1), 8 (2019)
4. H Chalabi, S Barik et al. “Synthetic Gauge Field for Two-Dimensional Time-Multiplexed Quantum Random Walks”, *Phys. Rev. Lett.* 123, 150503 (2019)
5. S Dutta, EA Goldschmidt, S Barik et al. “An Integrated Photonic Platform for Rare-Earth Ions in Thin-Film Lithium Niobate”, *Nano letters* 20 (1), 741-747 (2019)
6. S Barik et al. “A topological quantum optics interface”, *Science* 359 (6376), 666-668 (2018)
7. S Dutta, T Cai, MA Buyukkaya, S Barik et al. “Coupling quantum emitters in WSe 2 monolayers to a metalinsulator-metal waveguide” *Appl. Phys. Lett.* 113 (19), 191105 (2018)
8. JM Howard, EM Tennyson, S Barik et al. “Humidity-induced photoluminescence hysteresis in variable Cs/Br ratio hybrid perovskites”, *The journal of physical chemistry letters* 9 (12), 3463-3469 (2018)
9. Y Xu, EM Tennyson, J Kim, S Barik et al. “Active Control of Photon Recycling for Tunable Optoelectronic Materials”, *Advanced Optical Materials* 6 (7), 1701323 (2018)
10. S Barik et al. “Two-dimensionally confined topological edge states in photonic crystals”, *NJP* 18 (11), 113013 (2016)
11. K Lim, C Ropp, S Barik et al. “Nanostructure-induced distortion in single-emitter microscopy”, *Nano Letters* 16 (9), 5415-5419 (2016)
12. K S Alee, S Barik et al. “Förster energy transfer induced random lasing at unconventional excitation wavelengths”, *Appl. Phys. Lett.* 103, 221112 (2013)

1

¹The research works published in 1,6 and 10 are similar to the content presented here in the dissertation. The rest of the publications are unrelated and different.

Chapter 1: Introduction

1.1 Brief Overview

After its discovery, the topological insulator in condensed matter system [1, 2] gained significant interest for its potential applications. Then the concepts were translated to optics, giving rise to topological photonics [3, 4]. The conceptual framework of band topology from condensed matter has successfully been applied to photonic systems at microwave frequencies in various photonic crystal architectures [3, 6–8, 60]. Efforts are underway to extend these results into the optical regime, and there have been notable achievements, for example the realization of topologically protected edge states with near-infrared light in silicon ring resonator arrays [9, 10] and visible light in fused silica photonic crystal fibers [11, 12]. One particularly intriguing phenomena observed with such materials is that they exhibit electronic edge states that can travel along the edge in one direction without scattering even in the presence of impurities. This is due to the fact that band topologies are a property of the entire system and not a local property, and so local perturbations cannot alter the topology of the system.

A major motivation to introduce topologically protected edge states into photonic systems at optical frequencies is that they could potentially be incorporated

into photonic integrated circuits which could form an important element in future telecommunication technologies and reduce loss in the transmission of optical signals [13–15]. Looking beyond classical information processing, it is conceivable to interface topologically protected edge states with quantum emitters to realize quantum information processing [16], or more generally a quantum internet [17], and to perform quantum simulation with photons [18, 19], for example giving rise to fractional quantum Hall states [20].

The benefit of being able to interface topological light with quantum emitters is that this can realize strong interactions between photons with directional control. Although photons are by themselves essentially non-interacting, it is possible to introduce effective interactions through intermediaries such as cavities [21, 22], atoms [23–25] or quantum dots [26–28]. Numerous theoretical studies have explored ways to realize topological states of light in photonic systems [29, 30, 32–35], but to my knowledge none have led to the proposal of a readily realizable system in an all-dielectric substrate which has topological edge states in three dimensions and can interface directly with quantum emitters and other nanophotonic elements. For example, many of the structures considered theoretically use an array of rod-like elements, but the electromagnetic modes of these systems cannot be confined unless the ends are capped, for example with metals which are inherently dissipative at optical frequencies, and so cannot be used as a waveguide. Although recent experimental results have demonstrated chiral modes in one-dimensional photonic waveguides interfaced to emitters [36–38], these modes are not topologically protected, so it would be difficult to extend to two dimensions as would be necessary for on-chip routing

of light. The photonic crystal architecture we propose allows the integration of edge states that are topologically protected in two dimensions which can interface with quantum emitters and is confined with dielectric materials. Another notable aspect of this system is that it does not require any magnetic fields or magnetic materials to realize topological edge states [60].

Moreover, controlling light-matter at the single-photon level is at the heart of quantum optics, and plays a central role in quantum information applications. One way to control these interactions is by engineering the dielectric environment, which can modify the emission and absorption of a quantum emitter. In addition, proper design of the dielectric environment can create chiral modes of light that lock polarization and momentum. When coupled to quantum emitters, these chiral modes can control the directionality of spontaneous emission and modify photon-mediated interactions [96]. This control opens up new opportunities to tailor light-matter quantum states such as entangled spin states [109] and photonic clusters states [110].

Nanophotonics provides an alternate platform to engineer chiral light-matter coupling in a compact and scalable chip-integrated device. While chiral light-matter interactions have been successfully realized in waveguides [37], nanofibers [36], and millimeter-scale bottle resonators [111, 112], the application of these ideas to optical resonators that can strongly enhance coupling between emitters and photons, has remained elusive. This is partly due to the complications in designing resonators with chiral/helical properties. This is mainly because of the challenges in designing chiral resonators while maintaining small mode volumes, minimizing bending losses

and the susceptibility of the nanophotonic devices to fabrication disorders. However, A topological resonator could enable strong chiral light-matter interactions in a compact chip-integrated device and provide robustness against disorder, a major problem for nanophotonics in general.

Meanwhile, the field of topological photonics has emerged as a new paradigm to create a photonic structure with robustness against deformation [4,58]. In particular, in photonic crystals, this approach has been useful in realizing sharp bends and zigzag structures, without requiring fine-tuning of system parameters [29,100].

To that aim, in this thesis, I examine different nanoscale photonic crystal structures with triangular holes that sustains topological edge states which can couple to a quantum emitter in a chiral fashion. Structures like this can be fabricated with popular dielectric materials like Si or GaAs, which can be incorporated into photonic devices for reflectionless transport of light. We chose photonic crystals as the platform to realize topological edge states because of the flexibility they offer to engineer their band structures [39,40]. This property is critical in realizing non-trivial band topologies. Moreover, they allow the realization of nanophotonic structures ranging from optical cavities [41,42] to waveguides [44,76] with well understood nanofabrication technologies and techniques in slab materials, where the in-plane confinement is provided by photonic band gaps and out-of-plane confinement is provided by total internal reflection at the dielectric-air interface. Furthermore, dielectric nanophotonic structures such as Gallium Arsenide (GaAs) can be readily integrated with other nanophotonic elements, such as epitaxially grown quantum dots [45,46,69] and cold atom systems [156–159].

1.2 Outline of Thesis

In Chap. 2, we present an all-dielectric photonic crystal structure that supports two-dimensionally confined helical topological edge states. The topological properties of the system are controlled by the crystal parameters. An interface between two regions of differing band topologies gives rise to topological edge states confined in a dielectric slab that propagates around sharp corners without back-scattering. Three dimensional finite-difference time-domain calculations show these edges to be confined in the out-of-plane direction by total internal reflection. Such nanoscale photonic crystal architectures could enable strong interactions between photonic edge states and quantum emitters.

The application of topology in optics has led to a new paradigm in developing photonic devices with robust properties against disorder. Although significant progress on topological phenomena has been achieved in the classical domain, the realization of strong light-matter coupling in the quantum domain remains unexplored. In Chap. 3, we demonstrate a strong interface between single quantum emitters and topological photonic states. We demonstrate light-matter coupling between topologically protected photonic edge states and a quantum emitter. Our approach creates robust counter-propagating edge states at the boundary of two distinct topological photonic crystals. We demonstrate the chiral emission of a quantum emitter into these modes and establish their robustness against sharp bends. This approach may enable the development of quantum optics devices with built-in protection, with potential applications in quantum simulation and sensing.

In Chap. 4, we demonstrate a chiral coupling of a quantum emitter inside a topological photonic crystal resonator. Chiral nanophotonic components, such as waveguides and resonators coupled to quantum emitters, provide a fundamentally new approach to manipulate light-matter interactions. The recent emergence of topological photonics has provided a new paradigm to realize helical/chiral nanophotonic structures that are flexible in design and, at the same time, robust against sharp bends and disorder. Here we demonstrate such a topologically protected chiral nanophotonic resonator that is strongly coupled to a solid-state quantum emitter. Specifically, we employ the valley-Hall effect in a photonic crystal to achieve topological edge states at an interface between two topologically distinct regions. Our helical resonator supports two counter-propagating edge modes with opposite polarizations. We first show chiral coupling between the topological resonator and the quantum emitter such that the emitter emits preferably into one of the counter-propagating edge modes depending upon its spin. Subsequently, we demonstrate strong coupling between the resonator and the quantum emitter using resonant Purcell enhancement in the emission intensity by a factor of 3.4. Such chiral resonators could enable designing complex nanophotonic circuits for quantum information processing and studying novel quantum many-body dynamics.

In Chap. 5, I will provide the conclusion to the thesis along with potential applications of this work in the field of quantum nanophotonics.

Chapter 2: Topological Edge States in Photonic Crystals

2.1 Review

Topology is a ubiquitous concept in physics, ranging from electrons in solid state [1, 2], quantum degenerate gases [52, 53], and sound [54–57]. A key manifestation of topological physics is the presence of edge modes which are robust to local disorder. The prospect of using topological photonic materials for such robust propagation of light has attracted a great deal of interest [58, 59].

Topologically-protected edge states have been experimentally demonstrated in systems at microwave frequencies [60, 61] and optical frequencies, specifically in ring resonators [9, 10], and in coupled waveguides [11]. Subsequent work measured the invariants characterizing the topology of two-dimensional photonic systems [62]. Embedding quantum emitters into these optical frequency devices could generate strong optical non-linearities that exhibit new physical behavior. Theoretical work has shown that the interplay between emitters and chiral states results in intriguing phenomena such as many-body position-independent scattering [63], dimerization of driven emitters [64] and fractional quantum Hall states [20, 65, 66].

Strong light-matter interactions with optical emitters usually require the concentration of light to small mode-volume nanophotonic devices [67]. Two-dimensional

photonic crystals are one of the most promising nanophotonic platforms for this application because they confine light to less than an optical wavelength [68, 69]. Recently, several works have proposed all-dielectric photonic crystal structures where deformations open a gap in the Dirac cone dispersion to achieve non-trivial topological bands [29–31, 70]. However, these proposals consider the flow of light using two-dimensional numerical simulations with infinite extent in the third dimension and therefore do not address practical issues associated with propagation and confinement of light in a physically realizable crystal. A notable exception is the work of Wu *et al.* [29] which does consider structures of finite extent in the out-of-plane direction, but uses metallic mirrors to achieve confinement in this dimension. In this case the structure is no longer all-dielectric. Since metallic sheets are highly absorbing at optical frequencies, these mirrors would render the device extremely lossy. Thus, it would be highly desirable to create an all-dielectric topological photonic crystal.

In this chapter, we demonstrate that an all-dielectric topological photonic crystals can exhibit two-dimensionally edge states confined by total internal reflection in a dielectric slab. This design enables low-loss confinement of light in the third dimension. This structure addresses the challenge of experimentally realizing topological photonic crystals and enabling strong interactions with optical emitters. Our system exhibits spin quantum Hall physics for pseudo-spin photonic polarizations. As a result of time-reversal symmetry, the edge states are helical: edge states of opposite helicity travel in opposite directions. We utilize a honeycomb periodic structure with six-fold symmetry based on triangular holes. This structure ensures

a complete bandgap for transverse electric modes. Deformations of the unit cell that preserve its rotational symmetry change the topology of the structure. We show that interfacing two materials of different band topologies results in robust two-dimensionally confined edge states that can propagate around sharp bends.

2.2 Proposed structure

2.2.1 Honeycomb Lattice with Circular Holes

One idea is to implement our honeycomb-lattice-like photonic crystal structure with circular holes instead of triangular holes, as shown in Fig. 2.1(a). Although the band structure of the transverse-electric modes, as shown in Fig. 2.1(b), does give rise to a Dirac point, it turns out that it does not give rise to a band gap in the region of interest. The horizontal white dashed line shows the frequency at the Dirac point and the white dotted region encloses a range of wavevectors for which one of the bands crosses the frequency at the Dirac point, thus preventing the appearance of a band gap across the Brillouin zone even after perturbation, which is critical for realizing topological edge states. This can be avoided with the use of equilateral triangular holes, where a band gap is possible after perturbations to the system. This will be explored in detail next and will be a major point throughout this project.

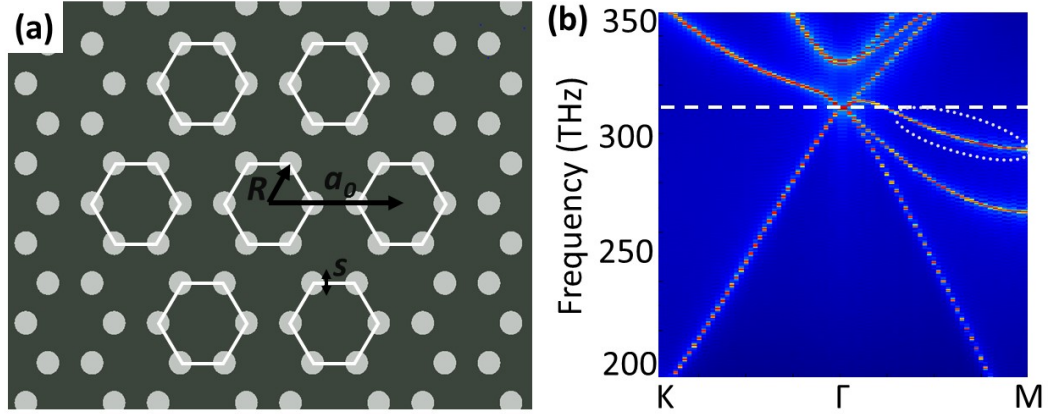


Figure 2.1: Band structure of a honeycomb lattice with circular holes : (a) Schematic of a honeycomb lattice made of circular holes, where the parameters a_0 is the lattice constant of the hexagonal clusters (white hexagons) which constitute a triangular lattice, R is the distance from the center of the cluster to the center of a circular hole within the cluster ($R = a_0/3$ in this case), and s is the diameter of the circular hole. (b) Band structure for transverse-electric modes of the structure shown in (a), showing the appearance of a Dirac cone at 312 THz (indicated by the horizontal white dashed line). White dotted ellipse shows one of the bands crossing the frequency at the Dirac point, which prevents the appearance of a band gap across the Brillouin zone after perturbation. Calculations were done with $a_0 = 350$ nm and $s = 140$ nm.

2.2.2 Honeycomb Lattice with Triangular Holes

Fig. 2.2 shows a schematic of our photonic crystal structure. The reason behind this geometry will be clear once we study the band structure of this system in the next section. Unlike the previous case : the lattice with circular holes, in this case there will be a complete band gap in the reciprocal space of the photonic lattice. The starting point is a honeycomb lattice made of equilateral triangular holes in a dielectric material as shown in Fig. 2.2(a). We can view this system as a triangular lattice with a basis consisting of two triangular holes, as is typically done in studies of graphene [71]. The black outline shows such a two-hole unit cell. Fig. 2.2(b) shows the first Brillouin zone (dashed line), which is a hexagon. We denote the high-symmetry points [161] by Γ , \tilde{M} and \tilde{K} . Alternatively, we can also view this structure as a triangular lattice of six-hole unit cells [white dashed hexagons in Fig. 2.2(a) which we call honeycomb clusters], where the relevant parameters are the lattice constant of the triangular lattice a_0 , the distance between the center of each cluster to the centroid of each triangular hole R , the length of each side of the equilateral triangular holes s , and the height of the dielectric material h . In the honeycomb lattice, the relationship $R = a_0/3$ holds. Fig. 2.2(b) shows the first Brillouin zone as a solid hexagon and Γ , M and K indicate the high symmetry points. Note that the first Brillouin zone for the six-hole unit cell is smaller than for the two-hole unit cell due to the larger real space unit cell area.

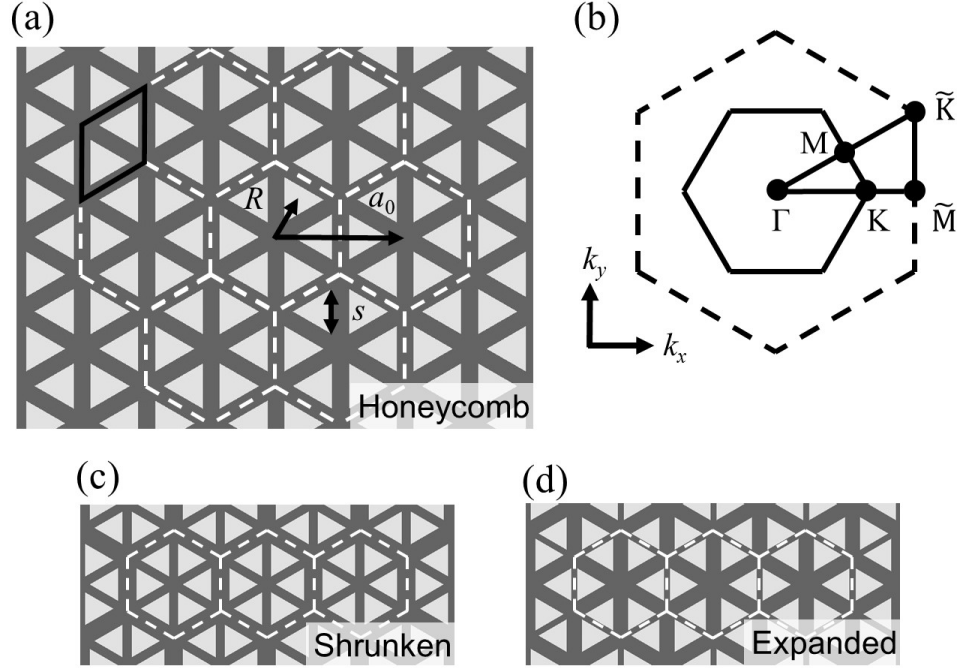


Figure 2.2: Schematic of our proposed honeycomb-lattice-like photonic crystal (a) Baseline structure of equilateral triangular holes arranged in a honeycomb lattice in a dielectric material. This honeycomb lattice can be viewed as a triangular lattice of two-hole unit cells (black solid rhombus), or alternatively as a triangular lattice of six-hole unit cells (white dashed hexagons), which we call honeycomb clusters with $R = a_0/3$. (b) First Brillouin zone for the six-hole (solid) and two-hole (dashed) unit cells. The letters indicate high-symmetry points. (c) [and (d)] Same structure as in (a) except that $R < a_0/3$ ($R > a_0/3$), which we call shrunken (expanded) clusters.

2.3 Band structure for TE modes

We first analyze the band structure of this photonic crystal in the two-hole unit cell picture using three-dimensional numerical finite-difference time-domain calculations (Lumerical FDTD Solutions). We perform simulations using GaAs as the dielectric substrate, with index of refraction taken from Ref. [73]. The parameters we use are $a_0 = 445$ nm, $s = 140$ nm, and $h = 160$ nm, which are typical dimensions for photonic crystal structures [46, 74, 75]. We focus on the transverse-electric-like modes of the system where the electric field at the symmetric plane of the system lies in-plane. Fig. 2.3(a) shows the band structure of the honeycomb lattice corresponding to Fig. 2.2(a) along the high-symmetry points of the Brillouin zone. The gray region indicates the portion of the band structure above the light line where there are no guided modes confined in the dielectric material of finite thickness [76]. There is a Dirac point at the \tilde{K} point, indicated by the red arrow in Fig. 2.3(a), located below the light line. Near this Dirac point, we can modify the topological properties of the photonic crystal by changing the ratio R/a_0 [29]. However, these perturbations also change the symmetry of the lattice and so we can no longer use the rhombus-shaped two-hole unit cell to construct the band structure. Instead, we use the hexagonal six-hole unit cell to construct the band structure without destroying the rotational symmetry of the system.

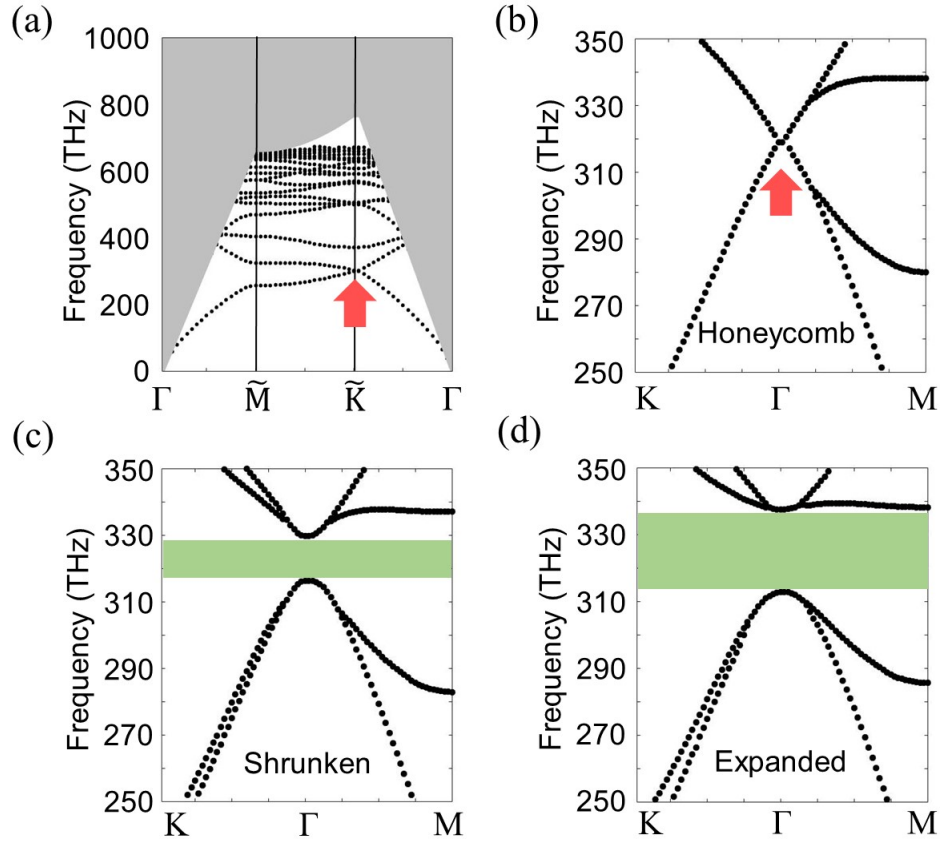


Figure 2.3: Band structures show opening and closing of a band gap around the Dirac point as we perturb the lattice. (a) Band structure of the honeycomb lattice in the two-hole unit cell picture. The gray area represents the region above the light line, where light can leak out of the plane. A Dirac point exists at the \tilde{K} point (red arrow) and is below the light line. (b),(c) and (d) Band structure calculated with the six-hole unit cell with honeycomb clusters ($R = a_0/3$), shrunken clusters ($R = 0.91 \times a_0/3$), and expanded clusters ($R = 1.09 \times a_0/3$) respectively. The red arrow indicates the Dirac point, and the green areas represent the band gap.

2.3.1 Band Folding

We obtain the band structure for the six-hole unit cell by appropriate band folding of the bands obtained from the two-hole unit cell (Appendix A). Although both Brillouin zones share the same Γ point, the \tilde{K} and \tilde{K}' points for the two-hole unit cell [71] become folded over onto the Γ point of the six-hole unit cell to form a doubly-degenerate Dirac point at 319 THz (which corresponds to 940 nm) as indicated by the red arrow in Fig. 2.3(b).

2.3.2 Perturbation to the system parameters

We perturb this system by varying R with respect to a_0 to get clusters that are shrunken ($R < a_0/3$) or expanded ($R > a_0/3$) as shown in Figs. 2.2(c) and (d) respectively. Figs. 2.3(c) and (d) show the corresponding band structures specifically for $R = 0.91 \times a_0/3$ and $R = 1.09 \times a_0/3$ respectively. Increasing or decreasing the ratio R/a_0 about the honeycomb lattice opens a band gap at the Dirac point. In particular, the band gaps are 13 THz and 25 THz wide for the shrunken and expanded clusters respectively. By comparing the eigenstates at the Γ point for the expanded and shrunken structures, we see that the eigenstates are inverted between the two structures, indicating that the band topology changes as we tune the ratio R/a_0 (appendix A).

2.3.3 Band inversion

To further confirm the numerically observed band inversion, we also analytically study the system with a tight-binding model(Appendix A). The Hamiltonian of our system reduces to the Bernevig-Hughes-Zhang model for the quantum spin Hall effect [77], where the mass term changes sign when the clusters are shrunken and expanded around $R = a_0/3$. Consequently, the bands acquire non-zero Chern numbers that are the direct indication of non-trivial band topology. In this case, the polarization profile of the in-plane electric field acts as the pseudo-spin.

2.4 Topological edge states

2.4.1 Non-trivial topology

Non-trivial band topologies manifest themselves most dramatically in the form of guided topological edge states at the boundary between two gapped regions that have different band topologies. To confirm this, we perform three-dimensional simulations of the structure schematically shown in Fig. 2.4(a) using the same values for the parameters a_0 , s and h as previously. We examine topological edge states at an interface between one region composed of unit cells with shrunken clusters (13 clusters wide) and another region of expanded clusters (12 clusters wide). These two regions share a common band gap in bulk as shown in Figs. 2.3(c) and (d).

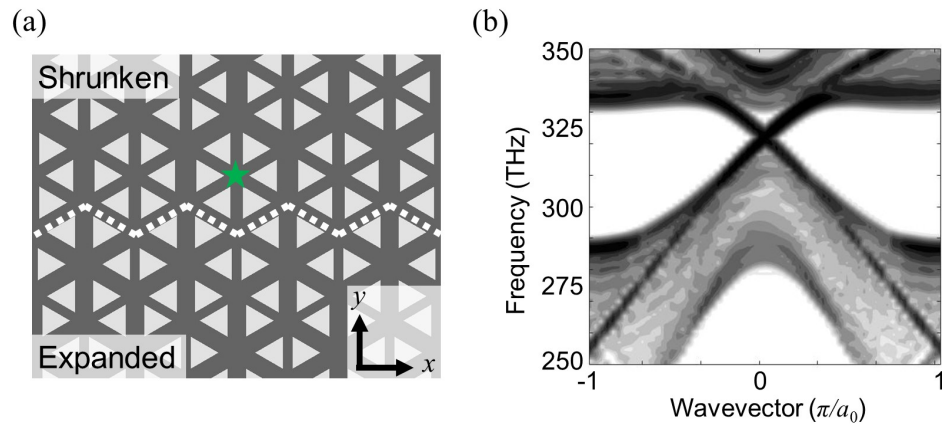


Figure 2.4: Schematic and band structure which gives rise to topological edge states. (a) Schematic of two regions with different band topologies. White dotted line marks the boundary between the two regions. The star (green) indicates the location where we placed a circularly-polarized electric dipole to excite topological edge states. (b) Corresponding one-dimensional band structure shows two bands crossing the band gap in bulk. The opposite group velocities in the crossing region indicate the existence of counter-propagating directional edge states.

2.4.2 One-dimensional band structure

Figure 2.4(b) shows the one-dimensional band structure along the x -direction. Note that introducing an interface creates two bands crossing the original bandgap of the individual regions. The two newly formed bands have opposite group velocities, indicating counter-propagating directional edge states.

2.5 Unidirectional propagation

2.5.1 Helical nature of edge states

The edge states in this system are helical, *i.e.*, the pseudo-spin degree of freedom controls the direction of propagation [1]. We verify the helicity of the edge states by exciting the system with a circularly-polarized electric dipole placed at the location indicated by the green star in Fig. 2.4(a). By choosing the excitation polarization to be positively (negatively) circularly polarized, we can selectively excite an edge mode propagating in the $-x$ ($+x$) direction (Fig. 2.5(b-i)[(b-ii)]). The excitation frequency is 320 THz (equivalent to a wavelength of 938 nm).

2.5.2 Topological confinement

Figs. 2.5(c) and (d) show the the electric field intensity distribution of the three-dimensional, vertically confined edge state[corresponding to Fig. 2.5(b-ii)] in xz and yz cross-sections respectively. The field is confined within the dielectric slab due to total internal reflection at the air-dielectric boundary. This proves that one

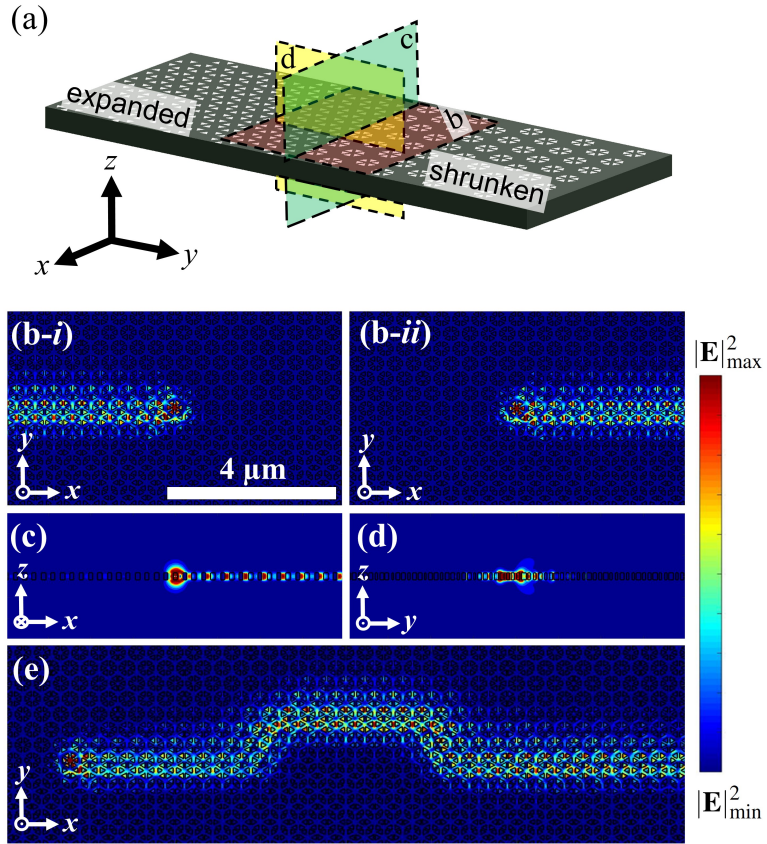


Figure 2.5: (a) Schematic diagram of the three-dimensional photonic crystal where the colored planes correspond to the cross-sections shown in (b), (c), and (d). (b-*i*) and (b-*ii*) Electric field intensities for a topological edge state excited with a positively and negatively circularly-polarized electric dipole show directional propagation in the $-x$ and $+x$ directions respectively. (c) and (d) Cross-section view along the xz and yz plane of the electric field intensity confirms that total internal reflection at the air-dielectric boundary prevents light from leaking out of the plane. (e) Electric field intensity for an edge state with four 90° bends show that light can propagate around defects without back scattering.

can realize topological edge states in three dimensions within dielectric materials at optical frequencies without significant out-of-plane loss.

2.6 Topological protection and robustness

One of the most distinguishing features of topological edge states is their robustness against perturbations. To test this robustness, we introduced four 90° bends to the structure as shown in Fig. 2.5(e). Excitation of the edge mode in this configuration shows that there is very little back-scattering along the entire path. Thus our edge states exhibit topological protection against certain types of disorder and defects, in contrast to chiral, but topologically-trivial, waveguide structures [36, 37].

2.7 Discussion

We note that the topological protection we obtain in the presence of time-reversal symmetry differs in an important respect from that of electronic quantum spin Hall systems. The general classification of topological insulators reveals that the Z_2 topological invariant describing the latter requires that $T^2 = -1$, where T is the time-reversal symmetry operator. The minus sign is a particular feature of fermionic systems. In contrast, Maxwell's equations (and other bosonic systems) obey $T^2 = 1$. This symmetry taken alone does not afford any topological protection in two dimensions.

However, we can construct a pseudo' time-reversal symmetry operator based

on the (C_{6v}) crystal symmetry of the lattice which obeys $T^2 = -1$ [29]. While this assures that the bulk may be classified according to a Z_2 topological invariant, gapless edge modes are not guaranteed since this symmetry is broken at the boundaries. This symmetry breaking can mix the counter-propagating edge states and open a mini-gap in the edge mode [78]; in a quantum spin Hall system, this would be akin to a magnetic impurity at the edge of the system. Apparently, in our realization this symmetry breaking is weak since we do not observe a gap in the edge states [Fig 2.4(b)]. We can decouple the pseudo-spin degrees of freedom up to linear order in \mathbf{k} near the Γ point. By considering these degrees of freedom as being completely decoupled, we can characterize the topology of the system by a stronger Z spin Chern number given by the difference of the Chern numbers for each pseudo-spin [79].

Chapter 3: Chiral coupling of a single photon inside a Topological Photonic Crystal Waveguide

3.1 Review

The discovery of electronic quantum Hall effects has inspired remarkable developments of similar topological phenomena in a multitude of platforms ranging from ultra cold neutral atoms [83, 84] to photonics [58, 85] and mechanical structures [86–88]. Like their electronic analogs, topological photonic states are unique in their directional transport and reflectionless propagation along the interface of two topologically distinct regions. Such robustness has been demonstrated in various electromagnetic systems, ranging from microwave domain [60, 89] to the optical domain [90, 91], opening avenues for a plethora of applications, such as robust delay lines, slow-light optical buffers [92], and topological lasers [93–95], to develop optical devices with built-in protection. While the scope of previous works remains in the classical electromagnetic regime, a great deal of interesting physics could emerge by bringing topological photonics to the quantum domain. Specifically, integrating quantum emitters to topological photonics structures could lead to robust strong light-matter interaction [96], generation of novel states of light and exotic

many-body states [97–99].

In this chapter, we experimentally demonstrate light-matter coupling in a topological photonic crystal. We utilize an all-dielectric structure [29, 100] to implement topologically robust edge states at the interface between two topologically distinct photonic materials, where the light is transversely trapped in a small area, up to half of the wavelength of light. We show that a quantum emitter efficiently couples to these edge modes and the emitted single photons exhibit robust transport, even in the presence of a bend.

3.2 Fabricated structure

3.2.1 Device Design

Figure 3.1 shows a schematic of the device design. We begin with a honeycomb lattice of equilateral triangles exhibiting hexagonal symmetry as our baseline structure. This lattice is a triangular lattice of cells consisting of six equilateral triangular holes, indicated by the dashed line. We use a lattice constant of $a_0 = 445$ nm, an edge length of the equilateral triangle of $s=140$ nm, and a slab thickness of $h = 160$ nm. R defines the distance from the center of a cell to the centroid of a triangle. In this structure a perfect honeycomb lattice corresponds to $R = a_0/3$.

With these parameters we obtain doubly degenerate Dirac cones at 319 THz (940 nm). We form the two mirrors by concentrically expanding or contracting the unit cell.

We create topologically distinct regions by deforming the unit cell of the pris-

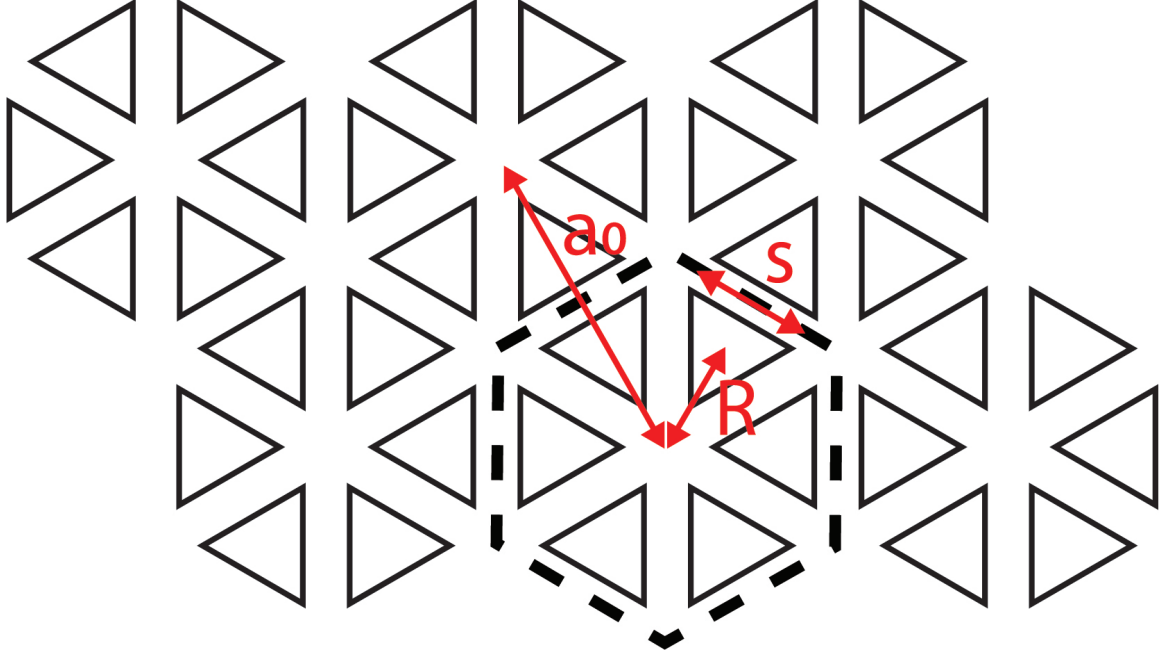


Figure 3.1: Design of honeycomb-like photonic crystal.

tine honeycomb lattice. On one side of the lattice, we concentrically shift the triangular holes by increasing R to $1.05a_0/3$, thereby shifting all the triangular holes in an individual cell outward. This deformation results in creation of a bandgap(Fig. 3.2 C). On the other side, we decrease R to $0.94a_0/3$, which pulls the holes towards the center resulting in the band structure with similar bandgap but with different topological properties(Fig. 3.2 D).

3.2.2 SEM image

Fig. 3.2 A shows the fabricated topological photonic crystal structure. The device is composed of a thin GaAs membrane with epitaxially grown InAs quantum dots at the center that act as quantum emitters (see Appendix B). The topological photonic structure is comprised of two deformed honeycomb photonic crystal lat-

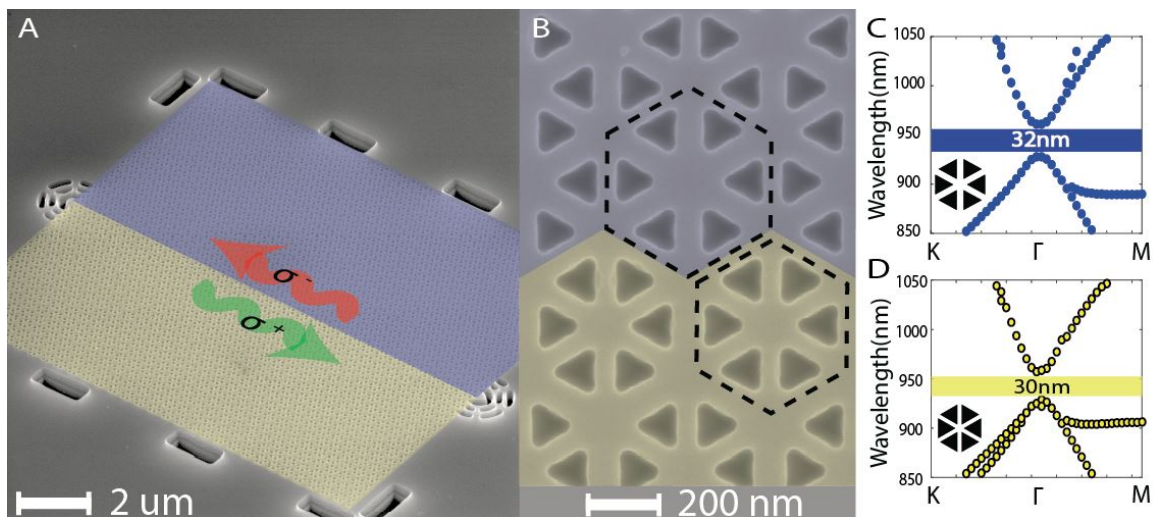


Figure 3.2: Fabricated device and band structure. (A) Scanning electron microscope image of the device composed of two regions identified by blue and yellow highlights, corresponding to two photonic crystals of different topological properties. The interface between the two photonic crystals supports helical edge states with opposite circular polarization (σ_+ / σ_-). Grating couplers at each end of the device scatter light in the out-of-plane direction for collection. (B) Closeup image of the interface. (C) and (D) show the band structures for the transverse electric modes of the two photonic crystals.

tices made of equilateral triangular air holes on a GaAs membrane [100]. Details regarding the fabrication and methods are described in Appendix B. Fig. 3.2B shows a closeup image of the interface, where the black dashed lines identify a single unit cell of each photonic crystal. In each region, we perturb the unit cell by concentrically moving the triangular holes either inward (yellow region) or outward (blue region).

3.2.3 Band structures : FDTD results

Fig. 3.2C-D shows the corresponding band structures of the two regions. Similar to calculations in chapter 2, we use FDTD methods to compute the shown band structures. The perturbations open two bandgaps exhibiting band inversion at the Γ point [29, 100]. Specifically, the region with compressed unit cell, highlighted in yellow, acquires a topologically trivial band gap, while the expanded region, highlighted in blue, takes on a nontrivial one. We design both regions so that their bandgaps overlap. Photons within the common bandgap cannot propagate into either photonic crystal. However, because the crystals have different topological band properties, the interface between them supports two topological helical edge modes, travelling in opposite directions, with opposite circular polarizations at the center of the unit cell.

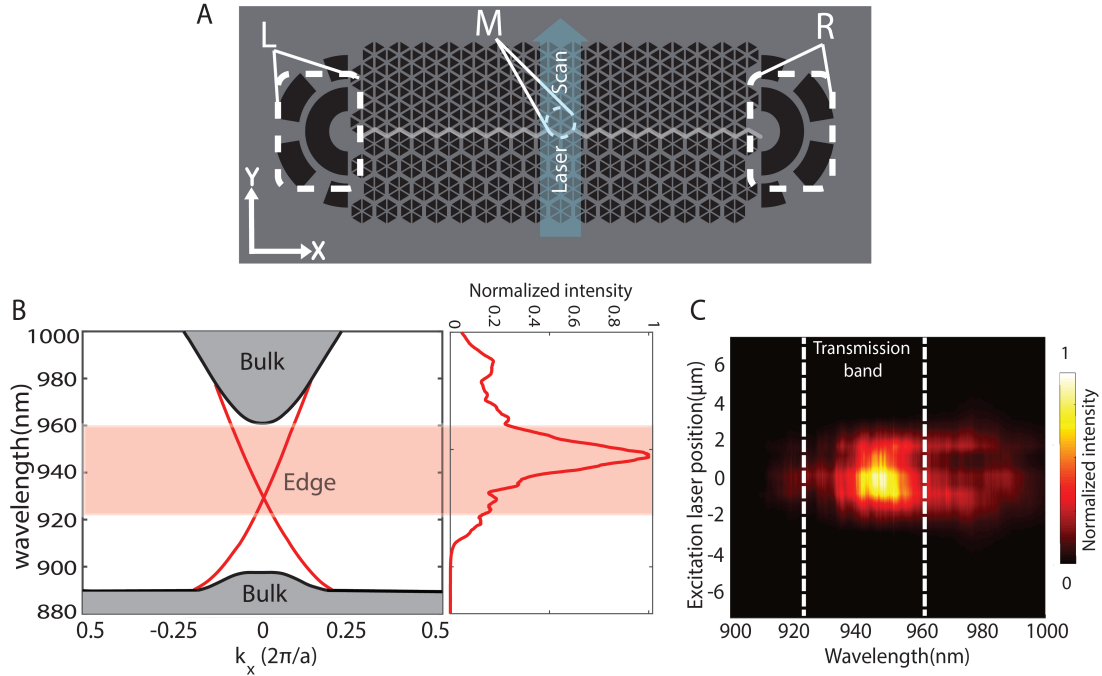


Figure 3.3: Transmission characteristics of the topological waveguide. (A) A schematic of the excitation scheme identifying the three relevant regions. (B) Simulated band structure of transverse electromagnetic modes of a straight topological waveguide. The grey region corresponds to bulk modes of the individual topological photonic crystals and red lines represent modes within the bandgap corresponding to topological edge states. The adjacent panel shows the measured spectrum at the transmitted end of the waveguide. The shaded region identifies the topological edge band. (C) Transmission spectrum at grating L as a function of the excitation laser position.

3.3 Waveguiding via edge states

3.3.1 Transmission of the waveguide

To show the presence of the guided edge mode, we measure the transmission spectrum. We illuminate the left grating (L) with a 780 nm continuous-wave laser using a pump power of 1.3W, and collect the emission from the right grating (R) (see Fig. 3.3A). At this power the quantum dot ensemble emission becomes a broad continuum due to power broadening, resulting in an internal white light source that spans the wavelength range of 900-980 nm. Fig. 3.3B shows the spectrum at the right grating, presented with the band structure simulation [100]. Light emitted within the topological band efficiently transmits through the edge mode and propagates to the other grating coupler, while photons outside of the bandgap dissipate into bulk modes.

3.3.2 Probing the guided modes at the interface

To confirm that the emission originates from guided modes at the interface between the two topological materials, we excite the structure in the middle of the waveguide (M), and collect the emission at the left and right grating coupler, which we independently calibrate (Appendix B). Fig. 3.3C shows the transmission spectrum collected from left coupler as a function of the laser spot position as we scan the laser along the y-axis across the interface indicated by blue arrow (see Fig. 3.3A). The spectrum attains a maximum transmission within the topological band when

the pump excites the center of the structure. When we displace the excitation beam, by approximately 1.5 microns along the y direction, the transmission vanishes, indicating that the photons are coming only from the waveguide.

3.4 Observation of chiral coupling of a single emitter

3.4.1 Zeeman effect

A key feature of topological edge modes is the chiral nature of the coupling between the helical topological edge mode and the quantum emitter. Specifically, different dipole spins radiatively couple to opposite propagating helical edge states. To demonstrate this helical light-matter coupling, we apply a magnetic field in the out-of-plane (Faraday) direction on the entire sample. This field induces a Zeeman splitting in the quantum dot excited state [101]. This results in two non-degenerate states that emit with opposite circular polarizations, denoted as σ_{\pm} as described next (Fig. 3.5A). While this magnetic field does not play a role in the topological nature of the waveguide, it enables us to identify the polarization of the dipole by the frequency of emitted photons. By spectrally resolving the emissions we can identify the dipole spin and correlate it with the propagation direction of the emitted photon.

3.4.2 Polarization of Quantum Dots Under Magnetic Field

We first measured the photoluminescence from a bare QD in the bulk. With the application of magnetic field QD emission spectrum splitted into two branches with circularly polarized emission as shown in Figure 3.4. A and denoted by σ_{\pm} .

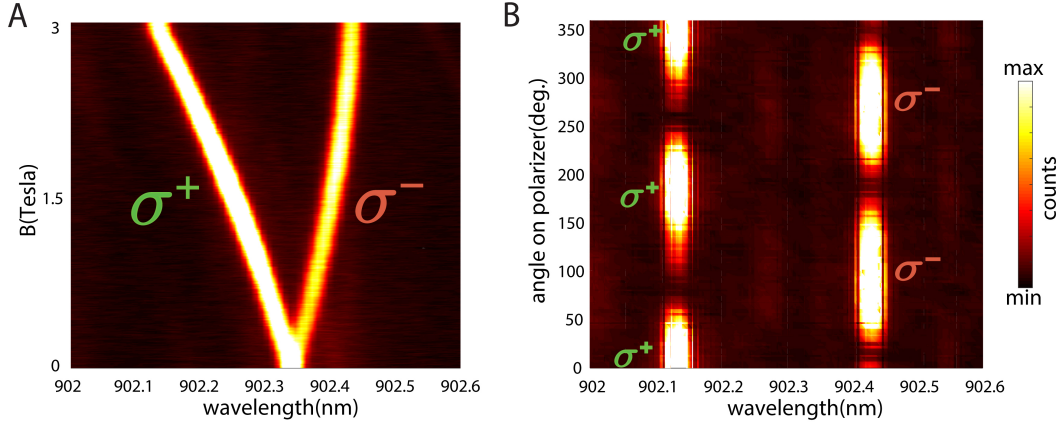


Figure 3.4: Polarization of quantum dot emission in bulk under magnetic field. (A) Splitting of single QD emission into σ_+ and σ_- exciton branches under application of magnetic field. (B) Verification of circular polarization of excitonic branches with polarization selective photoluminescence.

At a very high magnetic field of 3T the separation between two branches becomes 0.3 nm. at this stage to verify the selection rules we introduced a quarter wave plate and a polarizer before collecting the signal. Figure 3.4.B shows recorded photoluminescence obtained by rotating the polarizer angle. The antiphase relation between the two branches along with the detection scheme confirms that they are indeed circularly polarized in bulk under high magnetic field.

3.4.3 Chiral coupling of quantum dot emission into the waveguide

To isolate a single quantum emitter within the topological edge mode, we reduce the power to 10 nW, which is well below the quantum dot saturation power. Using the intensities of the collected light at the two ends, we calculate a lower bound on the coupling efficiency of 68% (Appendix B), defined as the ratio of the photon

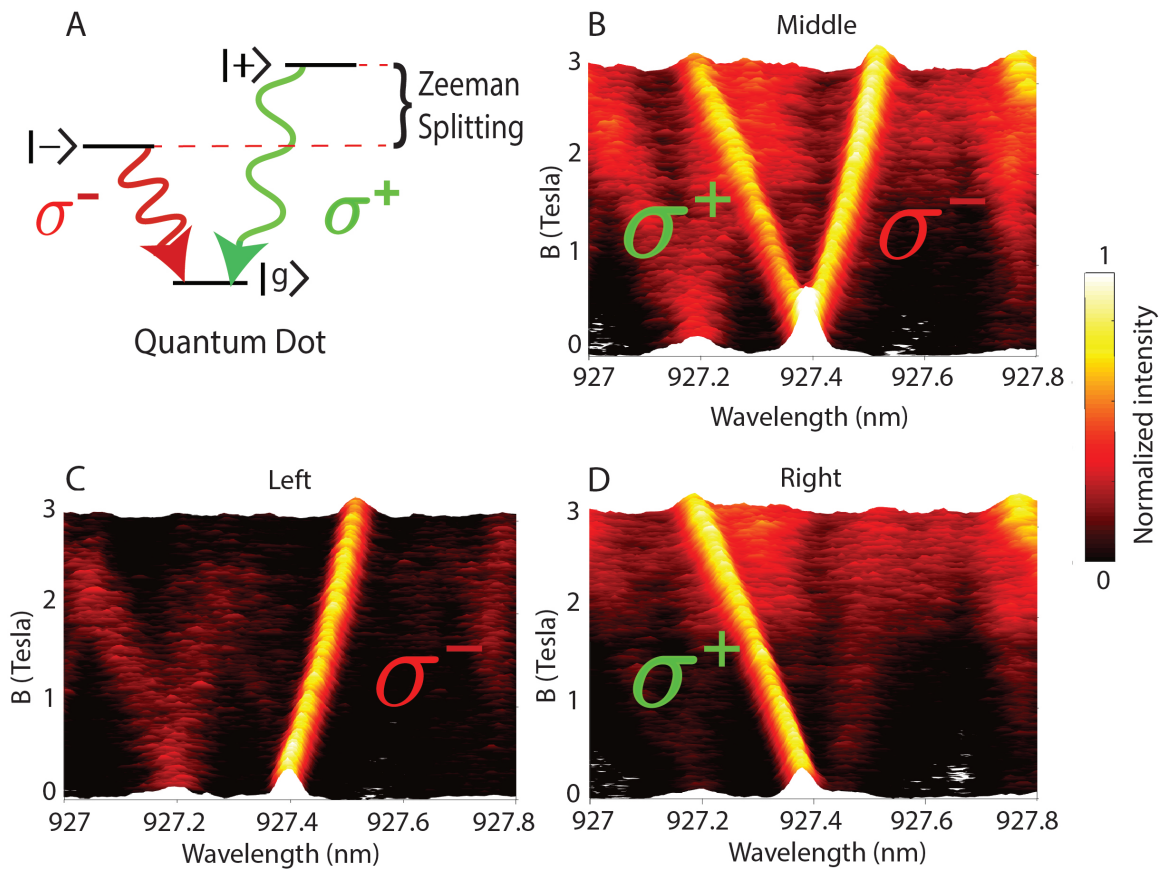


Figure 3.5: Chirality in a straight topological waveguide. (A) Schematic of quantum dot level structure in the presence of a magnetic field, and radiative transitions with opposite circular polarizations. (B) Emission spectrum collected from the excitation region as a function of magnetic field. (C) and (D) Transmission spectrum to left and right gratings, respectively.

emission rate into the waveguide to the total emission rate. This high efficiency is due to the tight electromagnetic confinement of the guided modes which enhances light-matter interactions. Figure 3.5B shows the emission spectrum as a function of magnetic field, where we collect the emission directly from point M indicated in the Fig. 3.3A. As the magnetic field increases, the quantum dot resonance splits into two branches corresponding to the two Zeeman split bright exciton states. We compare this spectrum to the one collected from left and right gratings (Fig. 3.5 C-D). At the left grating we observe only the emission from the σ_- branch, while at the right grating we observe only the σ_+ branch. These results establish the chiral emission and spin-momentum locking of the emitted photons, and provide strong evidence that the emitter is coupling to topological edge states that exhibit unidirectional transport. Such chiral coupling is in direct analogy to one dimensional systems [37, 102]. In contrast to one dimensional systems, the waveguided modes of our structure originate from two dimensional topology. As a result, the topological edge mode should exhibit robustness to certain deformations, such as bends.

3.5 Topological robustness

3.5.1 Waveguiding across a bend

In order to establish this topological robustness, we analyze the propagation of emitted photons in the presence of a bend. We introduce a 60 degree bend into the structure as shown in Fig. 3.6A, and perform measurements similar to those in Fig. 3.5. Again we observe that emitted photons propagate in opposite direction in a

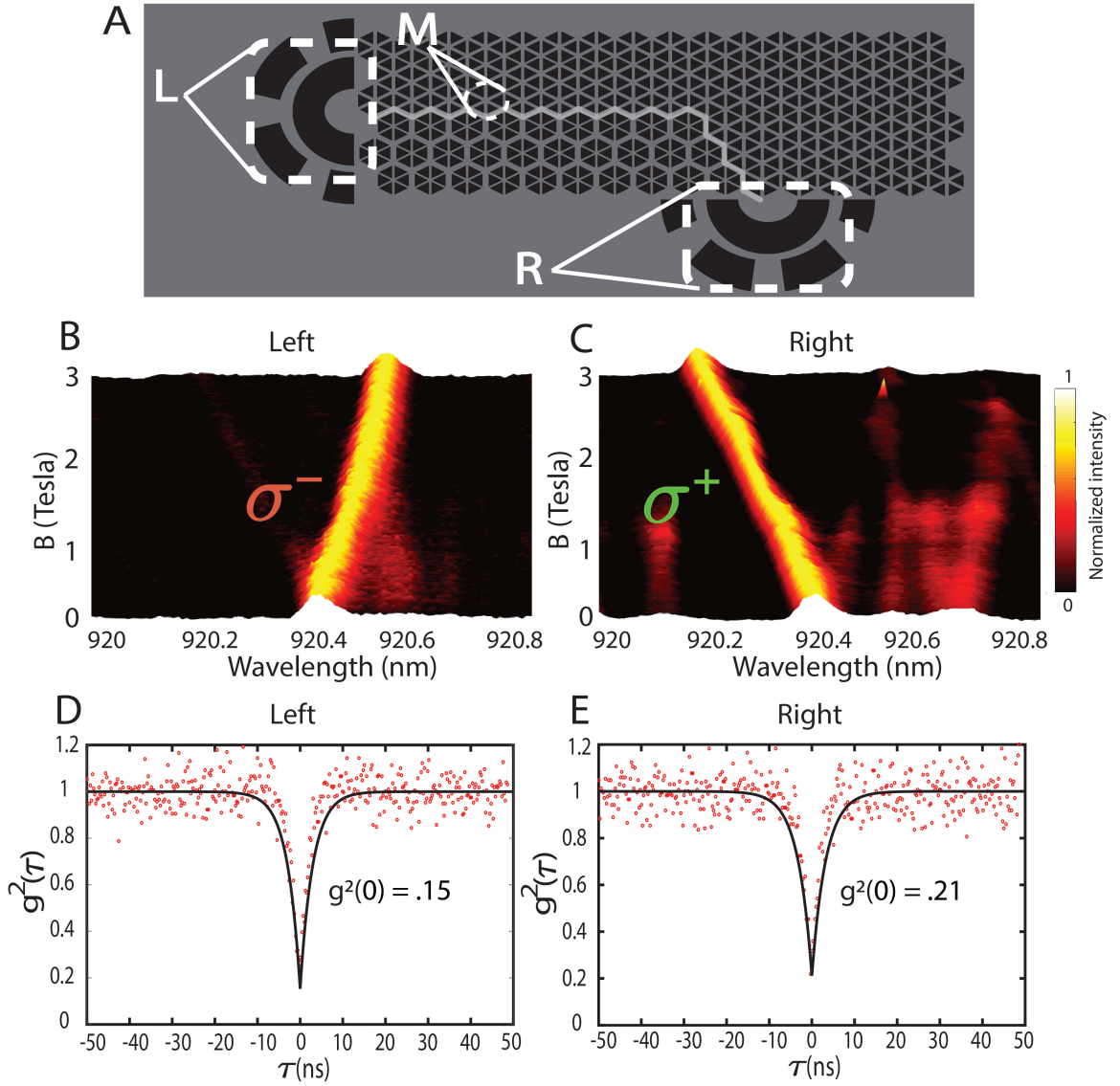


Figure 3.6: Robust transport in two dimensions along a bend. (A) Schematic of a modified topological waveguide with a bend. (B) and (C) Photoluminescence collected from position L and position R, respectively, showing only one branch of the quantum dot. (D) and (E) Second-order correlation measurement ($g^2(\tau)$) data obtained from point L and R, respectively, showing anti-bunching.

chiral fashion and arrive at the grating associated with their respective polarization (Fig. 3.6B-C). The preservation of the chiral nature of the emission demonstrates an absence of back-reflection at the bend, which would result in a strong signal for both polarizations at the left grating.

3.5.2 Routing single photon

We also confirm that these routed photons are indeed single photons by performing a second order correlation measurement for photons collected from both ends of the waveguide, which exhibits strong anti-bunching (Fig. 3.6D-E). We note that the robustness in this system is due to C_{6v} symmetry, and the boundary and disorder can break this symmetry and lead to backscattering of the edge modes.

3.5.3 Robustness to disorder

Next, we analyze the transmission of the edge mode to certain types of disorder and show that it maintains a good level of robustness. The full characterization of robustness, beyond numerical simulations and tight-binding model [103], requires further study.

The yellow and blue regions in Figure 3.2A represent the topologically distinct phases discussed above. Topological modes exist at the boundary, and are protected from any disorder which respects the six-fold crystal symmetry. Disorder that breaks this symmetry can lead to the backscattering of the edge modes. In fact, the formation of the interface itself can break this symmetry, albeit weakly.

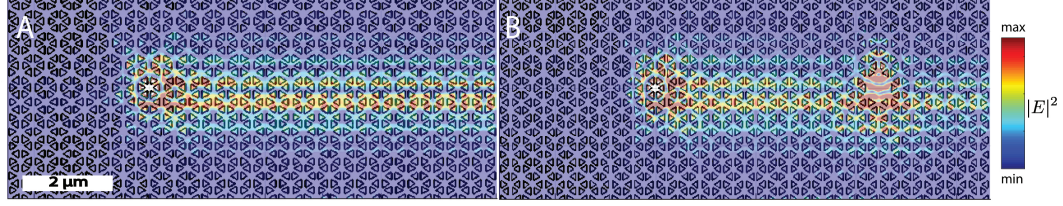


Figure 3.7: Effect of defects on the transmission of edge modes : Simulation showing a topological waveguide without a defect (A) compared to one with a large defect (B) that exhibits no backscattering.

Through extensive simulations, we have found that the zigzag interface in our device adequately preserves the crystalline symmetry, thereby minimizing the coupling between the counterpropagating edge modes. In Figure 3.7, we show simulations illustrating the robustness of the edge modes to a certain type of defect. The defect, an entire missing cell, breaks $C6v$ crystal symmetry. However, this defect does not adversely affect the transmission in the gapped region. We should note that the disorder seen in our device is considerably less severe.

3.6 Discussion

Once thought to be limited to the quantum Hall effect, the notion of topological insulating phases has revolutionized condensed matter physics and is the inspiration for topological photonic systems. These states are based on the fact that insulating Hamiltonians which obey certain combinations of symmetries (such as time-reversal) can be classified according to their topology. The photonic crystal considered here is described by a Z_2 topological invariant, which takes the value 0 (trivial phase) or 1 (topological phase). The physical manifestation of this is that between regions of

differing topology, protected edge modes are found. These modes cannot be coupled since such a term would violate the protected symmetry.

The photonic crystal considered in this work is an analog of a quantum spin Hall system for photons and is discussed in greater detail in [29]. The quantum spin Hall system exhibits topological protection that is based on time-reversal symmetry. In the context of the photonic crystal, the role of time-reversal symmetry is played by the six-fold rotational (C_{6v}) crystal symmetry of the hexagonal unit cell. In the energy range of interest, the band structure of the system is described by the Dirac equation, where the mass is controlled by the spacing of triangles in a hexagonal cluster. The topological Z_2 index reflects the sign of the mass, and is positive (negative) for compressed (expanded) regions. The topologically protected counterpropagating modes exist in the region at which the mass changes sign. In the context of the Dirac equation, these states are known as Jackiw-Rebbi states [165].

Chapter 4: Quantum optics with topological photonic crystal resonator

4.1 Review : Chiral quantum optics

Chiral propagation of light can fundamentally alter the way it interacts with matter. In particular, chiral light-matter interactions can control the directionality of spontaneous emission and modify photon-mediated interactions between quantum emitters [96]. These capabilities in-turn enable engineering of novel quantum states such as entangled spin states [109] and photonic clusters states [110]. Chiral light-matter interactions based on polarization-momentum locking of evanescent fields have been achieved previously, for example, using optical fibers [102] and millimeter-scale bottle resonators [111, 112]. Chiral light-matter interactions have also been explored using purely opto-mechanical interactions [113–116]. Recently, nanophotonics has emerged as a versatile platform to engineer chiral light-matter coupling in a compact and scalable fashion. In particular, chiral/helical waveguides coupled to solid-state quantum emitters have demonstrated directional spontaneous emission [117, 118]. However, extensions of these ideas to realize strong coupling between a chiral resonator and a solid-state emitter have remained elusive. This

is mainly because of the challenges in designing a nanophotonic resonator while preserving polarization-momentum locking.

Recently, topology has emerged as a new paradigm to design chiral photonic structures [4]. In particular, an interface between two topologically distinct regions hosts edge states exhibit chiral/helical propagation of light where the photon's momentum gets locked to a pseudospin degree of freedom, such as polarization. These edge states have the additional benefit that they are robust to deformations and disorders. Specifically, they also allow propagation of light around sharp bends and defects without scattering [90, 119–123], which is essential to engineer compact resonators that exhibit chirality [124, 125].

In this chapter, we demonstrate a topological resonator that exhibits strong light-matter interaction. We realize this resonator by creating an interface between two valley-Hall topological photonic crystals. By using an inhomogeneously broadened ensemble of quantum emitters as a broad-band light source, we first establish that our resonator supports edge modes that extend throughout the length of the resonator. Subsequently, using a single quantum emitter and a chiral waveguide coupled to the topological resonator, we demonstrate chiral spontaneous emission where the direction of the emission depends on the polarization of the emitted light. Having established the chirality of our resonator, we finally proceed to demonstrate strong coupling between the quantum emitter and the topological resonator. Specifically, we use a magnetic field to tune a quantum emitter into resonance with the topological resonator and show Purcell enhancement of emission. Our results pave the way for explorations of strong interactions between multiple solid-state quantum

emitters coupled via a chiral nanophotonic resonator.

4.2 Proposed Structure

4.2.1 Valley-Hall topological photonic crystal

Our chiral resonator is based on a valley-Hall topological photonic crystal [126–131], composed of a honeycomb lattice of triangular holes with a lattice constant of ‘a’, as shown in Fig. 4.1a. The two triangular holes in each rhombic unit cell (dotted rhombus), have different sizes ($\frac{1.3a}{2\sqrt{3}}$ and $\frac{0.7a}{2\sqrt{3}}$), which leads to the opening of topological bandgaps, at the K and K’ points. Because of the time-reversal symmetry, the Berry curvature integrated over the entire Brillouin zone is zero. However, the Berry curvature at K and K’ valleys have opposite signs. Interchanging the two triangular holes in the unit cell (green and violet regions in Fig. 4.1) flips the sign of the Berry curvature at each valley. Therefore, by interfacing these two topologically distinct regions, we form a pair of counter-propagating edge states with opposite helicity at the boundary between the two topologically distinct regions (shown as an orange band in Fig. 4.1c). These edge states are transverse electric (TE) modes composed of an in-plane electric field and can be selectively excited by placing an emitter at specific position along the interface of the waveguide with suitable circular polarization (see Appendix C)

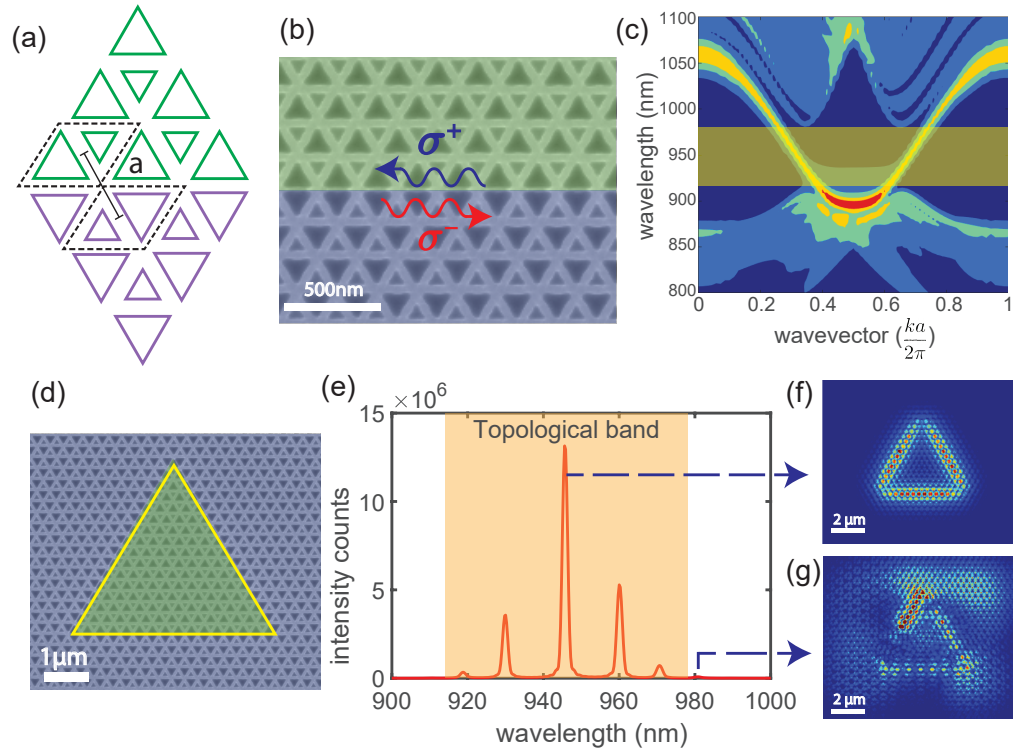


Figure 4.1: Valley-Hall topological photonic crystal resonator and FDTD simulation results: (a) Schematic of the topological interface showing two topologically distinct regions (violet and green), by interchanging the triangular holes sizes. Black dashed lines indicate the rhombic unit cells. (b) SEM image of the fabricated topological interface. (c) Simulated TE-band structure of the interface. The orange band highlights the edge band. (d) SEM image of a topological resonator shaped in the form of a super-triangle, with two topologically distinct regions (violet and green). (e) Simulated longitudinal modes of the resonator. As in (c), the shaded orange region corresponds to the topological edge band. (f) and (g) The electric field distribution of a resonator mode and a bulk mode.

4.2.2 Fabricated resonator structure

The topological edge states are robust against sharp bends of 60 and 120 degrees, which preserve the symmetry of the structure. This robustness enables them to form a resonator using a super-triangle (Fig. 4.1d), where the inside/outside of the super-triangle corresponds to two topologically distinct regions. Analogous to the one-dimensional edge states, this confined resonator structure hosts two counter-propagating modes with opposite helicity. We fabricated the resonator structure on a GaAs slab of thickness 160nm with an embedded layer of InAs quantum dots as quantum emitters. We patterned the structure using electron beam lithography followed by inductively coupled plasma reactive ion etching. We chose the lattice spacing of $a = 265\text{nm}$, such that the topological band gap coincides with the emission spectra of quantum dots. Appendix C provides a detailed description of fabrication steps.

4.2.3 Simulation results

The 3D Finite-difference Time-domain (FDTD) simulation for a resonator of length $13\mu\text{m}$ (50-unit cells) shows multiple longitudinal modes, separated by a free-spectral range (FSR) of 15nm (Fig. 4.1e). The calculated electric field profile of the resonator modes exhibits strong transverse confinement at the topological interface and extend over the super-triangle (Fig. 4.1f). Moreover, we do not observe any scattering at the three sharp corners of the resonator, indicating topological robustness. By contrast, the modes outside of the topological bandgap reside in the

bulk and are not extended along the resonator perimeter (see Fig. 4.1g). Since these modes are not protected, their frequency and their field profile are susceptible to the disorder.

4.3 Observation of topological resonator modes

To show the modes of the topological resonator, we excite the quantum dots at the tip of the resonator (shown in Fig. 4.2a) using a high-numerical aperture objective and a continuous wave laser at 780nm. We perform all measurements in a closed-cycle Helium cryostat, operating at 3K temperature. At this temperature, we use a high pump power of $100\mu\text{W}$ such that the quantum dots saturate and broaden to form a continuous internal white light source that probes the spectrum of the resonator. We collect the photoluminescence spectra from different points along the perimeter of the resonator (Fig. 4.2 b-d). We observe three peaks (within shaded grey regions) within the expected topological band which do not change when we move our collection point along the length of the resonator, indicating that these are the extended longitudinal modes of the topological resonator. Moreover, their free spectral range ($\approx 13\text{nm}$) matches closely with the simulation. The other peaks in the PL spectra change with the collection point, and therefore, correspond to the bulk modes of the photonic crystal structure.

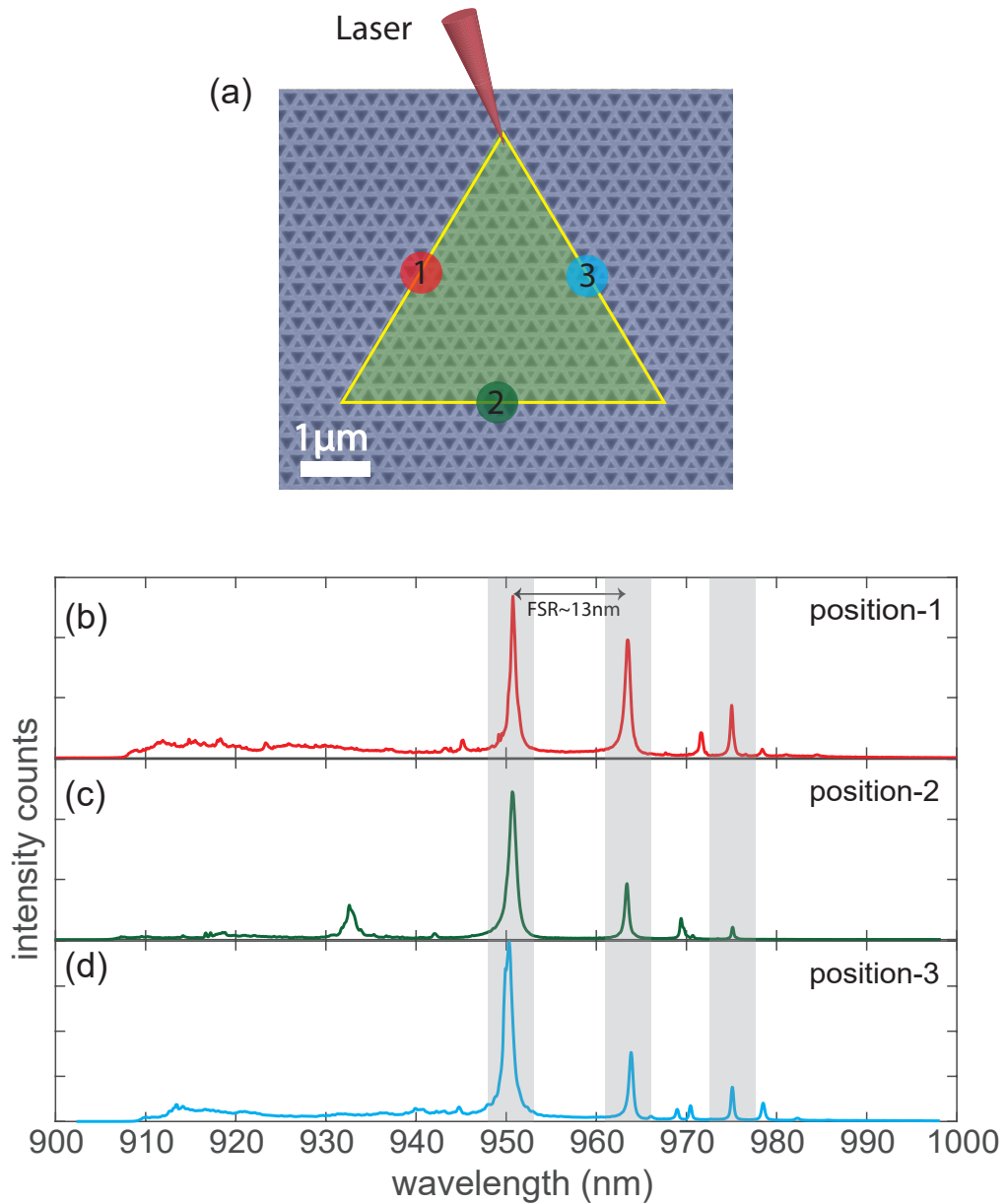


Figure 4.2: Topological waveguide-resonator system: (a) Schematic showing the excitation and collection points on a topological resonator device. Numbered marks show the position of collection spots. (b,c,d) The experimentally measured spectrum of a topological resonator from three different collection points along the length of the resonator. The peaks inside the grey regions correspond to the resonator modes.

4.4 Observation of chiral coupling of an emitter inside topological resonator

4.4.1 Waveguide-Resonator Hybrid Device : FDTD results

To probe the chiral coupling of an emitter to a topological resonator mode, we coupled the resonator to a helical topological waveguide, which is similarly designed (Fig. 4.3a). In this experiment, we excited the quantum dots at the point A on the resonator and collected the emission from the ends of the waveguide through the grating couplers. In order to analyze the chirality of the resonator mode, we numerically calculate the Poynting vector for the coupled resonator-waveguide device. Figure 4.3b shows the Poynting vector when the system is excited with a right circularly polarized dipole (σ_-). We observe that the electric field travels clockwise around the super-triangle, and then again chirally couples to the right of the waveguide. Due to time reversal symmetry, when the system is excited with a left circularly polarized dipole, we see the electric field travels anti-clockwise along the super-triangle, before exiting to the left of the waveguide (Fig. 4.3c). Note that the clockwise/anti-clockwise mode of the resonator couples to the right/left-going waveguide mode, respectively. This is due to the fact that the region below the waveguide has the same topology as the inside of the super-triangle, and therefore, the helicity is preserved at the boundaries. Here, we emphasize that the above mentioned polarization-momentum locking is dependent on the spatial position of the quantum dot with respect to topological interface.

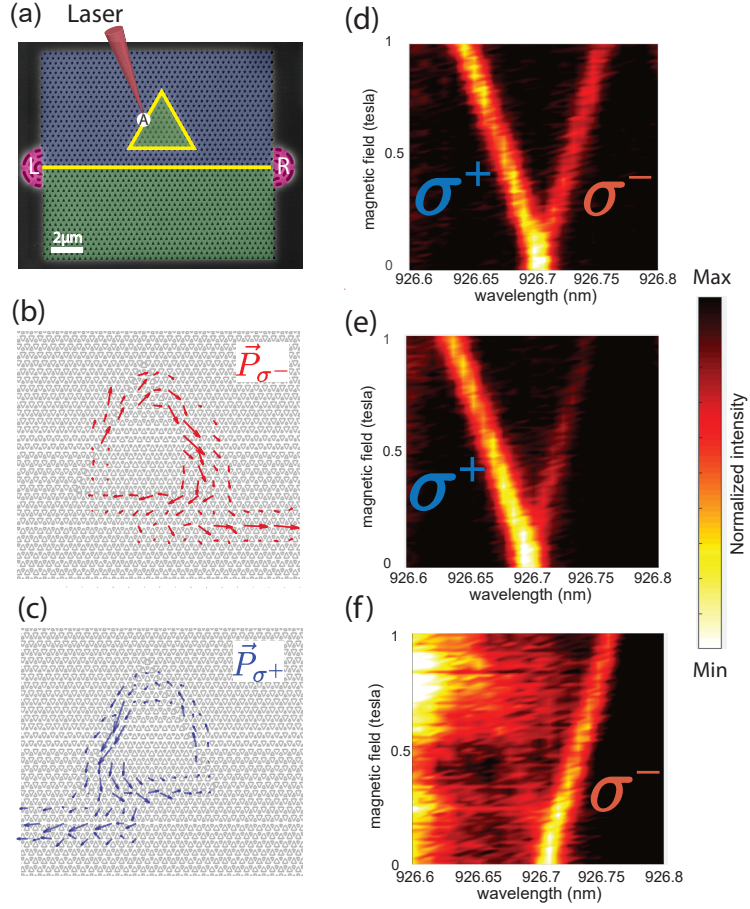


Figure 4.3: Chiral waveguide-resonator-emitter coupling: (a) SEM image of the topological resonator coupled with a topological waveguide, terminated by two grating couplers (pink shaded half-circles). The yellow line indicates the interface between two topological regions, highlighted in green and violet. Point A indicates the point of excitation. (b,c) Simulated Poynting vector profile along the perimeter of the resonator-waveguide system, when the system is excited with a right circularly-polarized dipole and left circularly-polarized dipole respectively. (d,e,f) The measured PL signal, as a function of the magnetic field strength, collected from point A, Left grating, Right grating, respectively.

4.4.2 Chiral coupling

To experimentally distinguish the chirality of the emitter-resonator-waveguide coupling, we perform a photoluminescence measurement on device shown in Fig. 4.3a. Specifically, we use two degenerate dipole transitions of the QD which are selectively coupled to the two helical edge states in the topological resonator. We apply a magnetic field on QDs, in a Faraday configuration, such that the Zeeman shift lifts the degeneracy of the two transitions [101]. This allows us to spectrally resolve the chiral nature of the light-matter interaction. Note that the helical nature of the resonator and the waveguide remains intact under such a magnetic field. We excite the sample at point A with a continuous wave 780nm wavelength laser at power $7\mu\text{W}$, such that individual QDs can be spectrally resolved. When the signal is collected at the point A (Fig. 4.3d), we observe both branches of the Zeeman split QD spectrum, corresponding to two oppositely-circular polarization. However, when we collect the signal from either of the grating couplers (Fig. 4.3(e)-(f)), we observe a single branch, as a signature of chiral coupling. We calculate near 89% directionality between the two gratings in this measurement.

4.4.3 Polarization-momentum locking

The above mentioned spin-momentum locking in this type of resonator system is dependent on the position of the quantum emitter along the waveguide. To affirm this fact, we excite a single resonator modes at different spatial points along the transverse direction with two circularly polarized dipoles and study the intensity

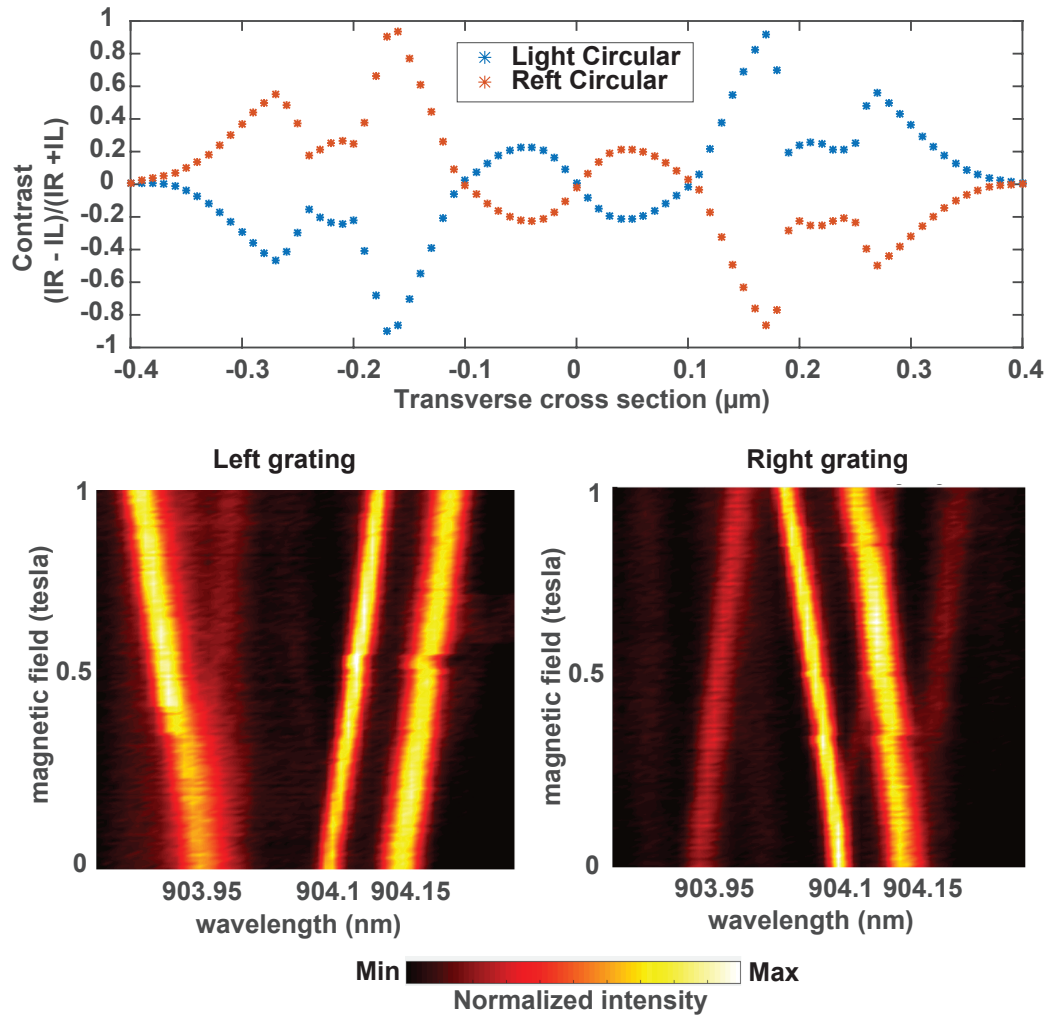


Figure 4.4: Position dependent spin-momentum locking : (a) Simulated results for contrast between the two grating with two different types of polarization excitation along the transverse direction of the waveguide. (b), (c) The measured PL signal, as a function of the magnetic field strength, collected from the Left grating, and Right grating, respectively.

variations at the two gratings. The results show that if the position of the emitting dipole is changed then the direction of the out-coupled light changes as shown in Fig. 4.4(a). Moreover, there are points of high chiral points where the magnitude of contrast reaches the maximum. Experimentally we further carry out PL measurements on another device. We find that within one excitation spot of the laser, depending on the position of the dot, the corresponding circular polarized emission will couple differently to the right/left propagating modes. This is apparent from Fig. 4.4(b) and (c) where the emission from a quantum dot at 903.95nm couples differently into the waveguide compared to the ones at 904.1nm and 904.15nm. Here, we want to note that even though the spin-momentum locking is similar to that found in ring resonators [96, 111, 112], these topological resonator modes have topological origin and arise from the fact that the two photonic crystals on either side of the triangular resonator have different band topology and therefore robust to bends and certain imperfection [130].

4.5 Intensity enhancement of a single emitter coupled to the resonator

In order to demonstrate that the quantum dots are coupled to the resonator, we measure their intensity as a function of cavity detuning. By scanning the magnetic field, one Zeeman branch of the QD spectrum can be tuned into the resonance of the topological resonator. Figure 4.5a shows the spectrum at two different excitation power. At high excitation power ($100\mu\text{W}$), the saturated QDs emission reveals the

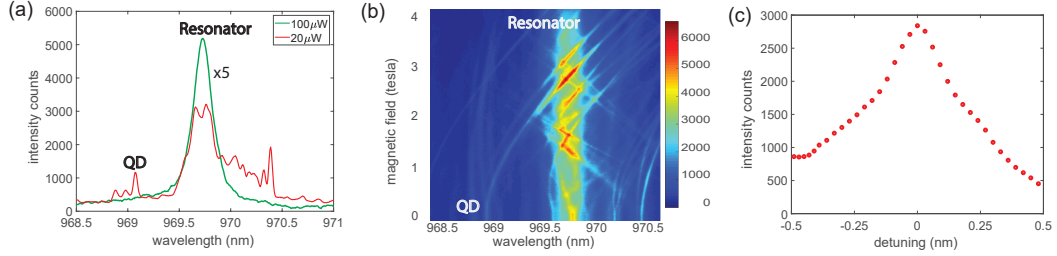


Figure 4.5: Purcell enhancement of a quantum emitter coupled to a topological resonator: (a) The measured PL, at zero magnetic field, exhibiting the QD and the resonator mode at high and low excitation power. (b) Enhancement of emitter’s PL, when the QD is tuned to the topological resonator, by scanning the magnetic field. (c) The intensity of the QD’s emission, as a function of detuning from the resonator mode.

cavity mode, as shown by the green curve. By decreasing the excitation power to $20\mu\text{W}$, the spectrum shows multiple individual quantum dot lines near the cavity resonance. Fig. 4.5b shows the measured spectra as a function of the magnetic field. As the magnetic field increases the quantum dots Zeeman split, and either the lower or upper branch crosses the cavity mode (depending on the initial detuning). The emission from the quantum dots is enhanced as they tune onto resonance with the cavity mode.

We focus on one particular dot labeled “QD” in Fig. 4.5a. This dot becomes resonant with the cavity at a magnetic field of 2.7 Tesla. To quantify the degree of enhancement, we fit the quantum dot to a Lorentzian function at each magnetic field and plotted its intensity as a function of detuning from the cavity (Fig. 4.5c). At zero detuning from the resonator line, we see a nearly threefold increment in the

count rates. From this emission enhancement, we estimate an intensity enhancement of 3.4.

Note: we used different measurement schemes for obtaining results depicted in different figures. We performed these measurements on different types of devices with different does array. Data presented in Fig. 4.2 4.3 4.5 has been taken from sample # D240_m3s2b_22 , # D240_m3s2b1d3_22, # D240_m3s2b1_21 respectively.

4.6 Summary

In summary, we demonstrate chiral light-matter interactions in a topological resonator. We use valley-Hall topological edge states to realize a helical resonator. Such a helical resonator is created at the interface of two distinct topological regions that supports two counter-propagating light modes with opposite polarizations. We show the chiral coupling of the resonator to a quantum emitter. Moreover, we achieve an intensity enhancement of 3.4 due to resonant coupling. These findings provide new approaches to study chiral quantum optics with potential applications in quantum information processing and quantum many-body physics.

Chapter 5: Conclusion and Outlook

In conclusion, we have proposed a new all-dielectric photonic crystal design and presented simulation results showing that three-dimensionally guided topological edge states at optical frequencies can be realized. The design parameters are amenable to implementation with well-established nanofabrication techniques. The simulations focus on GaAs as the dielectric substrate but the photonic crystal design principles that give rise to topological edge states are applicable to many other dielectric materials which can be fabricated with well-established nanofabrication techniques. The advantage of GaAs is that it can be integrated with quantum dots for example made of InAs whose charged states in the presence of magnetic fields have proven to be a promising solid-state qubit [136–138], and whose electronic transitions can emit circularly polarized light and can be interfaced with the helical topological edge states. Another potential substrate is InP, which can also be integrated with InAs quantum dots to realize topological edge states at telecommunication wavelengths [?, 139]. Aside from epitaxially grown quantum dots, defects in two-dimensional materials [80] can act as quantum emitters which emit circularly polarized light at optical frequencies [140–142], and these can be placed atop for example a silicon nitride photonic crystal [143, 144] nanofabricated

into the honeycomb-lattice-like structure described here. Other potential quantum emitters that could be integrated with topological edge states are defects in materials such as diamond [145, 146] or silicon carbide [147–149], which can be coupled to a photonic crystal [150] or even directly fabricated into photonic crystal structures [151–153]. Finally, cold atom systems could also be integrated with these photonic crystals [154–159]. Thus the demonstrated design should be applicable to a wide range of dielectric materials to realize topological photonics at optical frequencies and interfaced with various quantum emitters. With the further prospect of integration with various quantum emitters ranging from quantum dots [136–138], defects in two-dimensional materials [80] and diamond [145, 146], this system promises to open a new path to research in topological phenomena with optical systems.

Moreover, we also demonstrated coupling between single quantum emitters and topologically robust photonic edge states. The present approach opens up new prospects at the interface of quantum optics and topological photonics. In the context of chiral quantum optics, one can explore new regimes of dipole emission in the vicinity of a topological photonic structures and exploit the robustness of the electromagnetic modes [96]. Furthermore, in a chiral waveguide, photon-mediated interactions between emitters are location-independent [104]. This property could facilitate the coupling of multiple solid-state emitters via photons while overcoming scalability issues associated with random emitter position, enabling large-scale super-radiant states and spin-squeezing. Ultimately, such an approach could form a versatile platform to explore many-body quantum physics at a topological edge [105], create chiral spin networks [104, 106], and realize fractional quantum Hall

states of light [107, 108].

Additionally, building on the already demonstrated topological platform, next we studied a topologically robust and chiral interface between a photonic resonator and a quantum emitter. This platform could provide a robust and scalable pathway to engineer chiral light-matter interaction between multiple emitters coupled to a single resonator. It is important to note that topological design does not require fine tuning of system parameters, they are like LEGO! On the one hand, such resonators could enable the generation of entangled states of photons, mediated by chiral coupling of photons to quantum emitters [96], such as superradiant [132, 133] and cluster states [110]. On the other hand, one could conceive generating entangled states of several solid-state spins, mediated by the helical-circulating photonic modes [109]. In contrast to conventional waveguides, the mediated interaction strength between spins does not depend on the distance, since the emitters cannot form a mirror in a chiral interface. Ultimately, chiral and topological interfaces provide a new approach to study QED in a new regime [107, 108, 134, 135].

Appendix A:

A.1 Honeycomb Lattice with a Six-Site Basis and Band Folding

The photonic crystal we study is a modification of the usual honeycomb lattice. For the special case that the lattice parameters obey $R = a_0/3$, the standard honeycomb lattice is recovered (see main text for definitions). Typically, the honeycomb lattice is taken to be a triangular lattice with a two-site basis. For the general case $R \neq a_0/3$, it is convenient to consider the system as a triangular lattice with a six-site basis with primitive lattice vectors

$$\mathbf{a}_1 = (\sqrt{3}, 0) a, \tag{A.1}$$

$$\mathbf{a}_2 = (\sqrt{3}/2, 3/2) a, \tag{A.2}$$

where $a = \sqrt{3}R$. Figure A.1(a) shows the first Brillouin zones (FBZs) for both the two-site (dashed hexagon) and six-site (solid hexagon) bases.

The equivalence of these two descriptions can be verified by counting the total number of states in each case. The two-site basis is described by two bands over the FBZ of area A , giving a total number of states corresponding to an effective k -space area of $2A$. In the six-site case, each linear dimension of the FBZ is reduced by a

factor $\sqrt{3}$ and thus the area is $A/3$. Since there are six bands, this again gives a total effective area of $6 \times A/3 = 2A$.

In the case of graphene, it is well-known that the Dirac cones are located at the edges of the FBZ [labeled by \widetilde{K} in Fig. A.1(a)]. In the six-site basis, these degrees of freedom now reside at the zone center (Γ). The \widetilde{K} and Γ points are connected by a reciprocal lattice vector. The bands in Fig. A.1(c) can be obtained by folding along the vertical dashed lines in Fig. A.1(b) so that the \widetilde{K} is matched to Γ . At this point, the bands formerly at the two inequivalent Dirac points \widetilde{K} and \widetilde{K}' come together to form a doubly degenerate Dirac point. We will designate these degrees of freedom by a pseudospin (\pm) [29].

A.2 Tight-Binding Description of the Dispersion

The dispersion of our system near Γ ($\mathbf{k} = 0$) can be obtained by a tight-binding model. Following [160], we take a set of basis states for which the magnetic field profile is concentrated in a particular hole. The time-evolution of the system is characterized by ‘hopping’ to adjacent holes in the lattice. Typically, the application of tight-binding is limited to electronic systems in which electrons hop between weakly coupled atomic orbitals [163]. In the present context, the tight-binding method accurately captures the behavior of the band structure near Γ due to the fact that the near Γ , the band-structure is tightly constrained by the symmetries of the lattice. In particular, the tight-binding Hamiltonian \mathcal{H} naturally incorporates the C_{6v} symmetry of the lattice and the triangular holes. For the generic case that

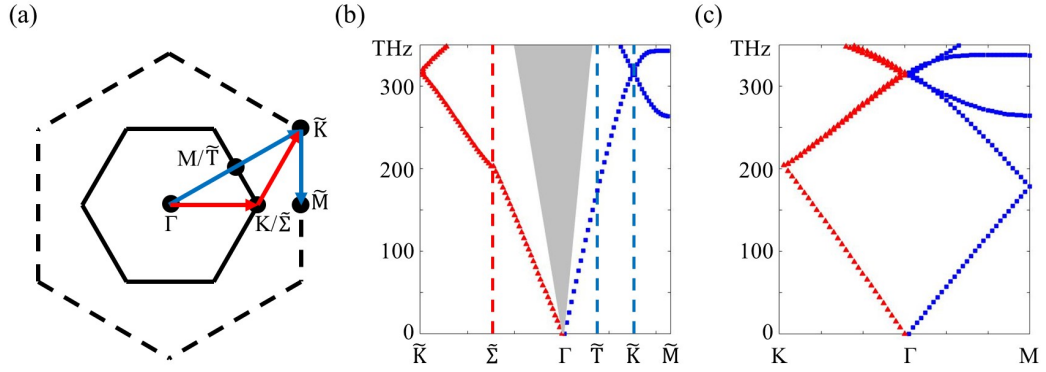


Figure A.1: Correspondence between the two-site and six-site bases : (a) Boundaries of the first Brillouin zone for the two-site (dashed hexagon) and six-site (solid hexagon) bases for the honeycomb lattice. (b) The band structure of the honeycomb lattice considered with a two-site basis. The labels on the horizontal axis corresponds to the high-symmetry points in k -space as designated in (a) [161]. The gray area is the area above the light cone where guided modes are not possible. The red triangles (blue squares) correspond to the red (blue) paths indicated in (a). (c) The band structure of the honeycomb lattice with a six-site basis as obtained by folding the band structure in (b) along the dotted vertical lines.

$a_0 \neq 3R$, the spectrum is gapped. For $a_0 = 3R$ corresponding to a honeycomb lattice, an additional C_{3v} symmetry ensures that the dispersion remain gapless at the Dirac point.

We describe our system as a triangular lattice with a six-site basis labeled A, B, C, \dots, F starting with the right-most site and progressing in a counter-clockwise manner (Fig. A.2). The states of our system $|A\rangle, |B\rangle, |C\rangle, \dots, |F\rangle$ are the Wannier functions for the system. For example, the state $|C\rangle$ describes an electromagnetic field configuration for which the out-of-plane magnetic field is centered on the C hole in each six-membered ring. In the bandwidth of interest, the magnetic field configurations can be written as linear combinations

$$|\Psi(\mathbf{k}, z)\rangle = \begin{pmatrix} \psi_A \\ \psi_B \\ \psi_C \\ \psi_D \\ \psi_E \\ \psi_F \end{pmatrix} e^{i\mathbf{k}\cdot\mathbf{r}}, \quad (\text{A.3})$$

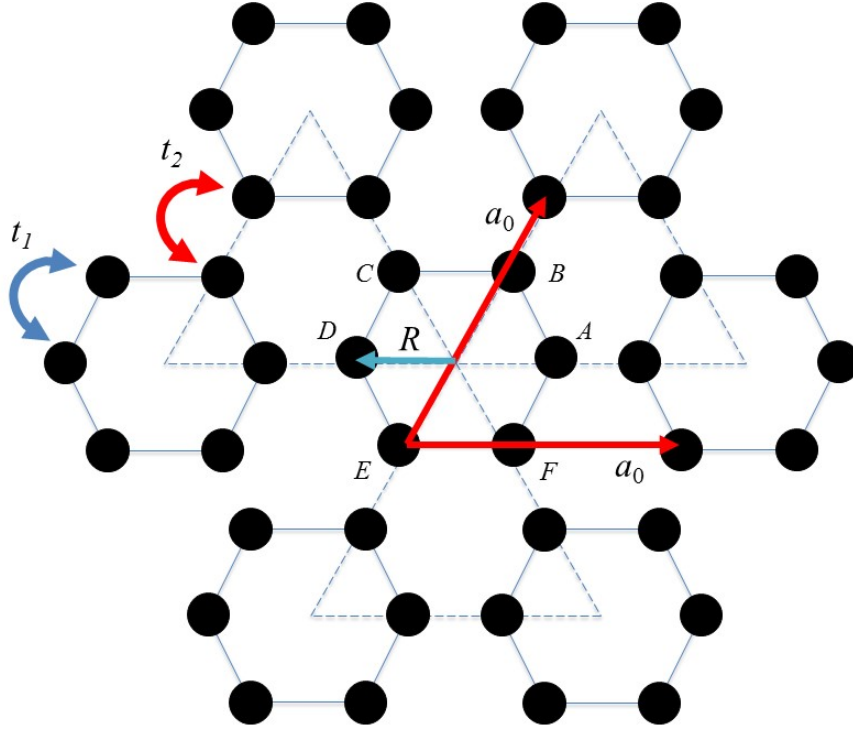


Figure A.2: Schematic of our lattice parameters and the labeling of the lattice sites for our tight-binding model. A cluster consists of six sites. Then the system is a triangular lattice of clusters with lattice constant a_0 . The distance from the centroid of each hole to the center of its cluster is R . The tunneling amplitudes t_1 and t_2 correspond to intra- and inter-cluster tunneling between the nearest neighbor holes. The labels A, B, C, D, E, F denote each lattice site making up the basis.

where $\mathbf{r} = (x, y)$ and Eq. (A.3) is written in the basis

$$|A\rangle = \begin{pmatrix} 1 \\ 0 \\ 0 \\ 0 \\ 0 \\ 0 \end{pmatrix}, |B\rangle = \begin{pmatrix} 0 \\ 1 \\ 0 \\ 0 \\ 0 \\ 0 \end{pmatrix}, \dots |F\rangle = \begin{pmatrix} 0 \\ 0 \\ 0 \\ 0 \\ 0 \\ 1 \end{pmatrix}. \quad (\text{A.4})$$

The action of the Hamiltonian operator is to evolve the state in time. Roughly, the matrix elements of \mathcal{H} indicate the field configurations which can evolve into each other on a time scale $\sim R/c$. On this time scale, only states which are localized to adjacent sites can evolve into each other appreciably and thus we only consider nearest-neighbor ‘hopping’. The Hamiltonian $\mathcal{H} = \mathcal{H}_1 + \mathcal{H}_2$ receives contributions from intra- and inter-cluster couplings, respectively. Intra-cluster hopping is characterized by a parameter t_1 and takes the form

$$\mathcal{H}_1 = -t_1 \begin{pmatrix} 0 & 1 & 0 & 0 & 0 & 1 \\ 1 & 0 & 1 & 0 & 0 & 0 \\ 0 & 1 & 0 & 1 & 0 & 0 \\ 0 & 0 & 1 & 0 & 1 & 0 \\ 0 & 0 & 0 & 1 & 0 & 1 \\ 1 & 0 & 0 & 0 & 1 & 0 \end{pmatrix}. \quad (\text{A.5})$$

Inter-cluster coupling is described by

$$\mathcal{H}_2 = -t_2 \begin{pmatrix} 0 & 0 & 0 & e^{i\mathbf{k}\cdot\mathbf{a}_1} & 0 & 0 \\ 0 & 0 & 0 & 0 & e^{i\mathbf{k}\cdot\mathbf{a}_2} & 0 \\ 0 & 0 & 0 & 0 & 0 & e^{i\mathbf{k}\cdot(\mathbf{a}_2-\mathbf{a}_1)} \\ e^{-i\mathbf{k}\cdot\mathbf{a}_1} & 0 & 0 & 0 & 0 & 0 \\ 0 & e^{-i\mathbf{k}\cdot\mathbf{a}_2} & 0 & 0 & 0 & 0 \\ 0 & 0 & t_2 e^{-i\mathbf{k}\cdot(\mathbf{a}_2-\mathbf{a}_1)} & 0 & 0 & 0 \end{pmatrix}. \quad (\text{A.6})$$

We introduce generalized plane wave states

$$|\Psi(\mathbf{k}, z)\rangle = \frac{1}{\sqrt{6}} \begin{pmatrix} 1 \\ z \\ z^2 \\ z^3 \\ z^4 \\ z^5 \end{pmatrix} e^{i\mathbf{k}\cdot\mathbf{r}}, \quad (\text{A.7})$$

where z is a complex number of unit magnitude whose phase is associated with angular momentum around the hexagonal clusters (or pseudospin, in the terminology of [29, 160]) and $\mathbf{k} = (k_x, k_y)$. Although the full rotational symmetry is broken by the crystal axis, the states corresponding to $z = e^{\pm i\pi/3}$ possess strong p -like character, while those with $z = e^{\pm i2\pi/3}$ have d -like character. This can be most easily seen by noting that the various states $|\Psi(z)\rangle$ are ‘sampled’ from continuous angular

wave functions as follows

$$|\Psi(z = e^{\pm i\pi/3})\rangle = e^{\pm i\theta} \rightarrow |p_{\pm}\rangle, \quad (\text{A.8})$$

$$|\Psi(z = e^{\pm i2\pi/3})\rangle = e^{\pm i2\theta} \rightarrow |d_{\pm}\rangle. \quad (\text{A.9})$$

The \pm labels the pseudo-spin degree of freedom. The geometry of the wavefunctions is clarified through the definitions

$$|p_x\rangle = \frac{1}{\sqrt{2}} (|p_+\rangle + |p_-\rangle), \quad (\text{A.10})$$

$$|p_y\rangle = \frac{1}{i\sqrt{2}} (|p_+\rangle - |p_-\rangle) \quad (\text{A.11})$$

where $|p_x\rangle$ is odd about the x -axis, etc. Similarly, we have

$$|d_{x^2-y^2}\rangle = \frac{1}{\sqrt{2}} (|d_+\rangle + |d_-\rangle), \quad (\text{A.12})$$

$$|d_{xy}\rangle = \frac{1}{i\sqrt{2}} (|d_+\rangle - |d_-\rangle), \quad (\text{A.13})$$

where $|d_{x^2-y^2}\rangle$ is a wave function whose maxima coincide with the x - and y -axes as $\theta = 0 \rightarrow 2\pi$, etc.

We now derive the spectra associated with these 4 states near Γ by expanding Eq. (A.6) to linear order in k_x and k_y . In this limit, the effective 4×4 Hamiltonian is block diagonal, and only states of the same pseudo-spin are coupled. The effective

Hamiltonian for the (+)-pseudo-spin is given by

$$\mathcal{H}_+ = \frac{\sqrt{3}}{2}t_2a(-k_x\sigma_x + k_y\sigma_y) + [t_2 - t_1 + \mathcal{O}(k_x^2 + k_y^2)]\sigma_z, \quad (\text{A.14})$$

in the $(|p_+\rangle, |d_+\rangle)^T$ basis. Similarly, in the $(|p_-\rangle, |d_-\rangle)^T$ basis we find

$$\mathcal{H}_- = \frac{\sqrt{3}}{2}t_2a(k_x\sigma_x + k_y\sigma_y) + [t_2 - t_1 + \mathcal{O}(k_x^2 + k_y^2)]\sigma_z. \quad (\text{A.15})$$

In both cases, we have performed a unitary transformation $U = e^{i\frac{\pi}{2}\sigma_z}$. We note that in the limit that the various honeycombs are completely decoupled, $t_2 \approx 0$ and Eqs. (A.14) and (A.15) reflect the fact that the p -states have a lower energy than the d -states. For $t_1 = t_2$, \mathcal{H}_+ and \mathcal{H}_- are characterized by a Dirac cone spectrum. For $t_1 \neq t_2$, the spectrum acquires a gap of size $|t_1 - t_2|$.

A.3 Topology and Edge States

In the previous section, we showed that a honeycomb structure can be described by a gapless Dirac Hamiltonian. When we introduce the lattice deformations, *i.e.*, shrinking/expanding, a gap opens which can be described a mass term ($m\sigma_z$). Here, we review the concept why the band inversion, *i.e.*, changing the sign of mass, results in having a topological edge at the boundary.

When the system is gapped, its topology can be characterized by a Chern

number for the pseudospins (\pm). A spin Chern number takes the form

$$\mathcal{C} = \mathcal{C}_+ - \mathcal{C}_-, \quad (\text{A.16})$$

where $\mathcal{C}_\pm = \pm \frac{1}{2} \text{sgn}(m_\pm)$, where m_\pm are the masses for the two pseudo-spins [162].

Thus, we have

$$\mathcal{C} = \text{sgn}(t_2 - t_1). \quad (\text{A.17})$$

Topologically-protected edge modes will exist between gapped regions with different \mathcal{C} 's, *i.e.*, any place that the quantity $t_2 - t_1$ changes sign.

In order to understand the edge state structure, we begin by considering \mathcal{H}_+ with a spatially varying mass. For concreteness, we consider the situation outlined in Fig. 4b in the main text. As we will see, edge states are localized to domain walls for which $m(x) = t_2 - t_1 \approx 0$. The edge states satisfy the Heisenberg equation of motion which, for \mathcal{H}_+ [Eq. (A.14)], is the Dirac equation. The Dirac equation corresponding to \mathcal{H}_+ is

$$[-i\hbar v (-\sigma_x \partial_x + \sigma_y \partial_y) + m \sigma_z] \Psi = E \Psi, \quad (\text{A.18})$$

where $v = \sqrt{3}t_1 a_0/2$ and E is the energy of the eigenstate Ψ .

Consider the geometry shown in Fig. 4(b) of the main text, which shows an area of shrunken hexagons above expanded hexagons. The system is described by a

mass which depends only on y , *i.e.*, $m(x, y) = m(y)$ and $m(0) = 0$ with

$$\frac{dm}{dy} < 0. \quad (\text{A.19})$$

In this case, the topologically protected solution

$$\Psi(y) = \chi \exp\left(\frac{1}{\hbar v} \int_0^y m(y') dy'\right), \quad (\text{A.20})$$

is an x -independent solution of the Dirac equation with zero energy where χ is a two-dimensional spinor. This is the celebrated Jackiw-Rebbi solution of the Dirac equation with a spatially varying mass [165]. The sign in the exponent of Ψ [Eq. (A.20)] ensures that the solution is normalizable. The edge state decays exponentially for both $y > 0$ and $y < 0$. The spinor χ obeys

$$\sigma_x \chi = \chi. \quad (\text{A.21})$$

Thus,

$$\chi = \frac{1}{\sqrt{2}} \begin{pmatrix} 1 \\ 1 \end{pmatrix}, \quad (\text{A.22})$$

in the $(|p_+\rangle, |d_+\rangle)^T$ basis. The full edge mode is described by

$$\Psi(x, y) = \frac{1}{\sqrt{2}} \begin{pmatrix} 1 \\ 1 \end{pmatrix} \exp\left(\frac{1}{\hbar v} \int_0^y m(y') dy'\right) e^{ik_x x}. \quad (\text{A.23})$$

Again, plugging into the Dirac equation gives an energy dispersion

$$E(k_x) = -\hbar v k_x. \tag{A.24}$$

Since the group velocity is given by $v = \frac{1}{\hbar} \frac{\partial E}{\partial k_x}$, this represents an edge state travelling in the $-x$ -direction. Indeed, we see that in Fig. 4(b-*i*) of the main text, the excitation of the $+$ -pseudospin leads to a left-moving edge state. Similarly, an edge state derived from the \mathcal{H}_- channel (opposite pseudo-spin) would travel in the $+x$ -direction.

A.4 Inversion of the Eigenstates

We examine the out-of-plane magnetic field eigenstates of the system at the symmetry plane ($z = 0$) corresponding to the Γ point for the shrunken and expanded clusters. The band structures for the shrunken and expanded cluster systems are shown in Fig. A.3(a) and (d) and are the same as Fig. 2(c) and (e) in the main text. The eigenstates corresponding to these band structures show that the eigenstates are inverted; by that we mean that *e.g.*, the eigenstate p_x (d_{xy}) shown in Fig. A.3(b) [A.3(c)] which appeared on the lower (upper) band for the shrunken cluster appears on the upper (lower) band for the expanded cluster as shown in Fig. A.3(f) [(e)]. This band inversion indicates that there is a change in the band topology, as discussed in the previous section on the tight-binding model.

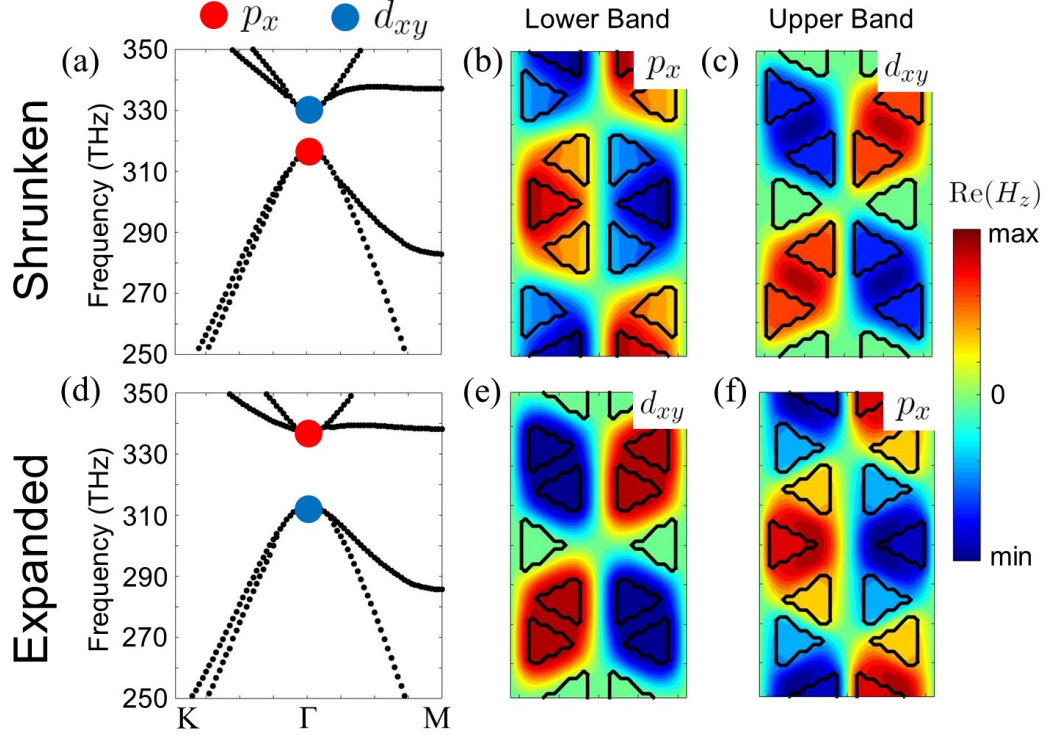


Figure A.3: Band inversion : (a) and (d) Band structures for the shrunken and expanded cluster systems, which are the same as Fig. 2(c) and (d) respectively in the main text, with a subset of the eigenstates indicated at the Γ point. (b) and (c) [(e) and (f)] Out-of-plane magnetic field eigenstates at the symmetry plane $z = 0$ of the lower and upper band for the shrunken (expanded) cluster system respectively. We see that *e.g.*, the eigenstate p_x for the lower band in the shrunken cluster system appears on the upper band for the expanded cluster system, which indicates a change in the band topology.

A.5 Polarization Pseudo-Spin of the Eigenstates

From Maxwell's equations, at the symmetry plane $z = 0$, the out-of-plane magnetic field eigenstates $p_x \hat{\mathbf{z}}$ and $p_y \hat{\mathbf{z}}$ lead to an in-plane electric field given by

$$\mathbf{E}_1 = \frac{i}{\omega \epsilon_0 \epsilon(\mathbf{r})} \nabla \times (p_x \hat{\mathbf{z}}) \quad \mathbf{E}_2 = \frac{i}{\omega \epsilon_0 \epsilon(\mathbf{r})} \nabla \times (p_y \hat{\mathbf{z}}), \quad (\text{A.25})$$

where $\mathbf{E}_i = E_{ix} \hat{\mathbf{x}} + E_{iy} \hat{\mathbf{y}}$ ($i = 1, 2$), $\epsilon_0 \approx 8.854 \times 10^{-12}$ Farad/m is the vacuum permittivity, and $\epsilon(\mathbf{r})$ is the position-dependent relative permittivity. The out-of-plane magnetic fields of the p_x and p_y eigenstates are shown in Figs. A.4(a) and (b), respectively. We see that the p_x and p_y modes are related by a $\pi/2$ rotation, so we have at the center of the cluster ($\mathbf{r} = 0$) the relation

$$\begin{pmatrix} E_{2x} \\ E_{2y} \end{pmatrix} = \begin{pmatrix} -E_{1y} \\ E_{1x} \end{pmatrix} \quad (\text{A.26})$$

From this we find the relation

$$\frac{i}{\omega \epsilon_0 \epsilon(0)} \nabla \times [(p_x \pm ip_y) \hat{\mathbf{z}}] = (E_{1x} \mp iE_{1y})(\hat{\mathbf{x}} \pm i\hat{\mathbf{y}}). \quad (\text{A.27})$$

This implies that at the center of the clusters the in-plane electric field polarization is either σ_+ - or σ_- -circularly polarized depending on the out-of-plane magnetic field eigenstates $\mathbf{p}_\pm = (p_x \pm ip_y) \hat{\mathbf{z}} / \sqrt{2}$ where $\sigma_\pm = (\hat{\mathbf{x}} \pm i\hat{\mathbf{y}}) / \sqrt{2}$. We can see this directly in Figs. A.4 (c) and (d), which show $\Delta\sigma \sim |E_+|^2 - |E_-|^2$ where $E_\pm = (E_x \mp iE_y) / \sqrt{2}$, characterizing the degree of circular polarization. In both

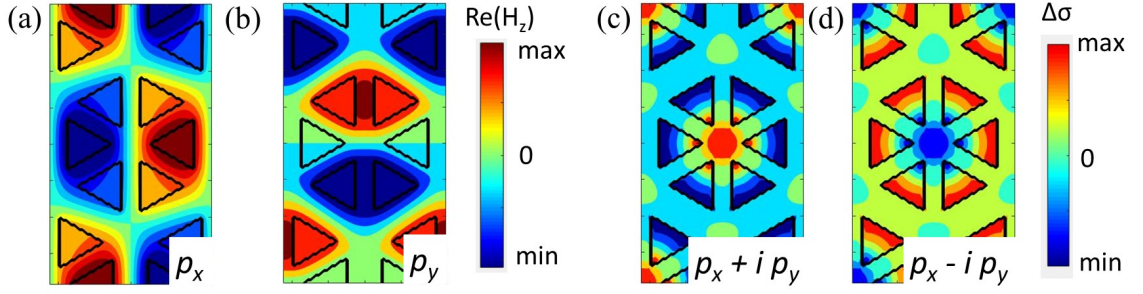


Figure A.4: Out-of-plane magnetic field and in-plane electric field polarization in a cluster of six holes outlined by black triangles. (a) and (b) depict the real part of the out-of-plane magnetic field (H_z) for the eigenstates p_x and p_y respectively. The colors indicate the strength of H_z . (c) and (d) show $\Delta\sigma \sim |E_+|^2 - |E_-|^2$, indicating the pseudo-spin nature of the bands excited at the Γ point with $p_x + ip_y$ and $p_x - ip_y$ modes, respectively.

cases we see that at the center the in-plane electric field is highly circularly polarized, except with opposite handedness. Thus the out-of-plane magnetic field eigenstates p_{\pm} have an associated in-plane electric field circular polarization of σ_{\pm} which act as pseudo-spins for this topological photonic crystal.

Appendix B:

B.1 Device Fabrication

To fabricate the device, we began with an initial wafer composed of a 160 nm GaAs membrane on top of 1 μm sacrificial layer of $\text{Al}_{0.8}\text{Ga}_{0.2}\text{As}$ with quantum dots grown at the center. The quantum dot density was approximately $50 \mu\text{m}^{-2}$. Based on the given quantum density and cross-sectional area of the waveguide, the probability of finding two dots in the structure with the same resonance is less than 0.7%. Thus, it is extremely unlikely in a given device for a photon emitted by one dot to be scattered by a second.

We fabricated the topological photonic crystal structure using electron beam lithography, followed by dry etching and selective wet etching of the sacrificial layer. We first spin-coated the wafer with ZEP520A e-beam resist, then patterned the structure using 100 keV acceleration voltage and developed the resist using ZED50 developer. After patterning, we used chlorine-based inductively coupled plasma etching to transfer the pattern on the GaAs membrane. We finally performed selective wet etching using HF acid to create a suspended structure with air on top and bottom. The rectangular structures in the periphery are included to facilitate undercut of the sacrificial layer.

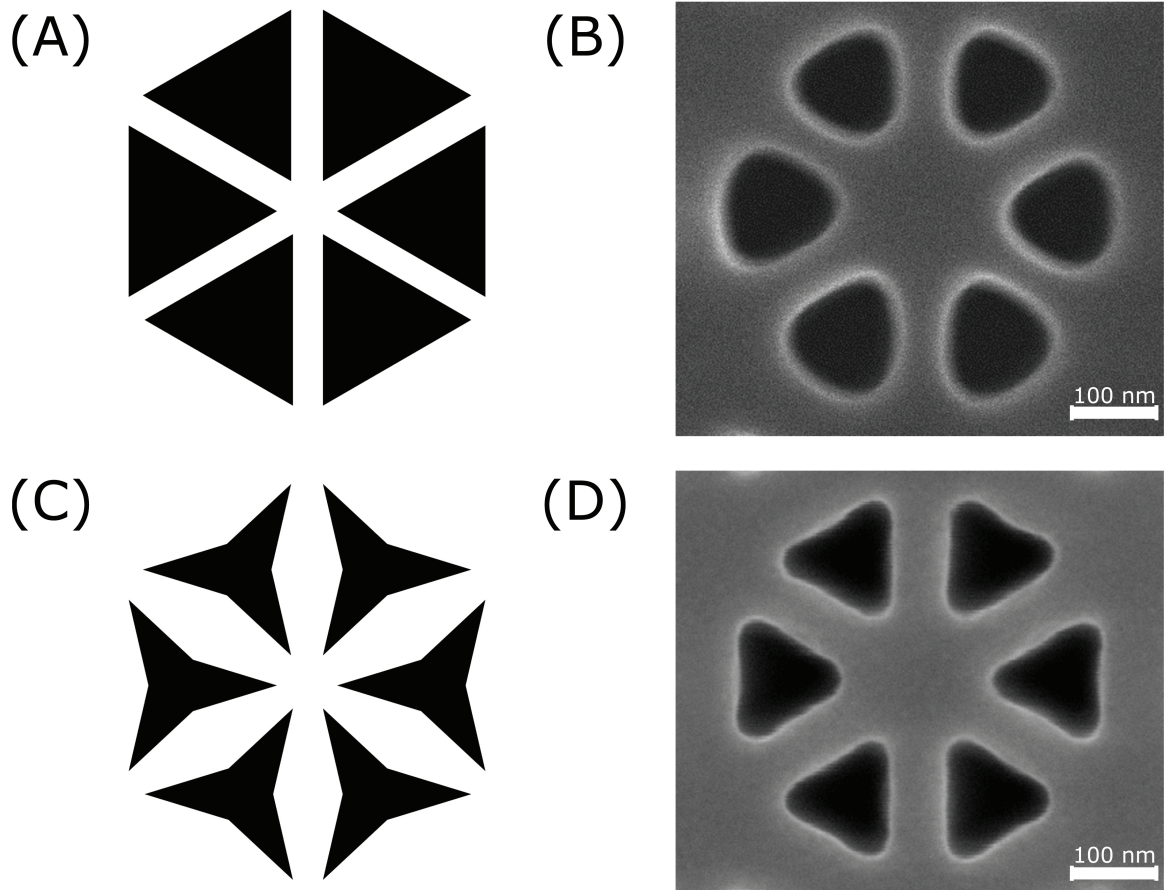


Figure B.1: Mask design for fabrication of triangles. (A) Layout of regular mask. (B) SEM image of rounded triangles resulted from use of regular mask. (C) Layout of modified mask; triangles are bent from edges to mitigate etching imperfections. (D) SEM image of sharp triangles fabricated with use of modified mask.

Sharp corners with straight side walls are essential to observe the topological helical edge modes. It is confirmed via simulation that triangles with rounded corners are detrimental for the device operation. However, even with highly directional dry etch, creating sharp features like triangles is challenging at such small length scales. We observed – by using a regular mask design (as shown in Figure B.1.A) – that etching causes widening of holes which eventually results in rounded corners much like a Reuleaux triangle (Figure B.1.B). We used a modified mask design to overcome this challenge. Triangles with shrunk edges shown in Figure B.1.C are used as a mask; this results in sharp triangles with edge lengths of 140 nm. Close up SEM image of final structure is shown in Figure B.1.D.

B.2 Experimental Setup

To perform measurements, we mounted the sample in a closed-cycle cryostat and cooled it down to 3.6 K. A superconducting magnet, contained within the closed-cycle refrigerator, surrounds the sample and applies a magnetic field of up to 9.2 T along the out-of-plane (Faraday) direction in order to generate a Zeeman splitting between the two bright excitons of the quantum dot. We performed all sample excitation and collection using a confocal microscope with an objective lens with numerical aperture of 0.8. We collected the emission and focused it onto a single mode fiber to perform spatial filtering. To perform spectral measurements, we injected the signal to a grating spectrometer with a spectral resolution of 7 GHz. For autocorrelation measurements, we used a flip mirror to couple the light

out of the spectrometer and processed the filtered emission using Hanbury-Brown Twiss intensity interferometer composed of a 50/50 beamsplitter, two Single Photon Counting Modules (SPCMs) and a PicoHarp 300 time correlated single photon counting system.

The quantum dots are less than 20 nm in diameter, while the laser spot size is approximately 0.4 μm . The density of quantum dots are $50 \mu\text{m}^{-2}$ which means that there are approximately 25 dots within the excitation spots. However, due to the large inhomogeneous broadening of the ensemble, each of these dots emits at a different wavelength. We isolate individual quantum dots by spectral filtering using a grating spectrometer with a resolution of 0.02 nm. The spectrometer selects the emission from only a single dot, as evidenced by the anti-bunching dip observed in Fig. 4D-E which dips below 0.5.

B.3 Grating Calibration

Since both left and right grating couplers are fabricated under similar condition they are identical in terms of coupling efficiency. To test this fact we calibrated them with respect to. the transmission spectrum of the topological waveguide. Figure B.2.A shows the different positions on the device. We shine an intense excitation beam of 780 nm with 1.5uW power at the center of the waveguide (M). At this high power all the quantum dots are saturated and emit a broadband spectrum ranging from 900-980nm. We collected the transmitted signal from left (L) and right grating (R). Figure S B.2.B shows almost equal counts coming from both

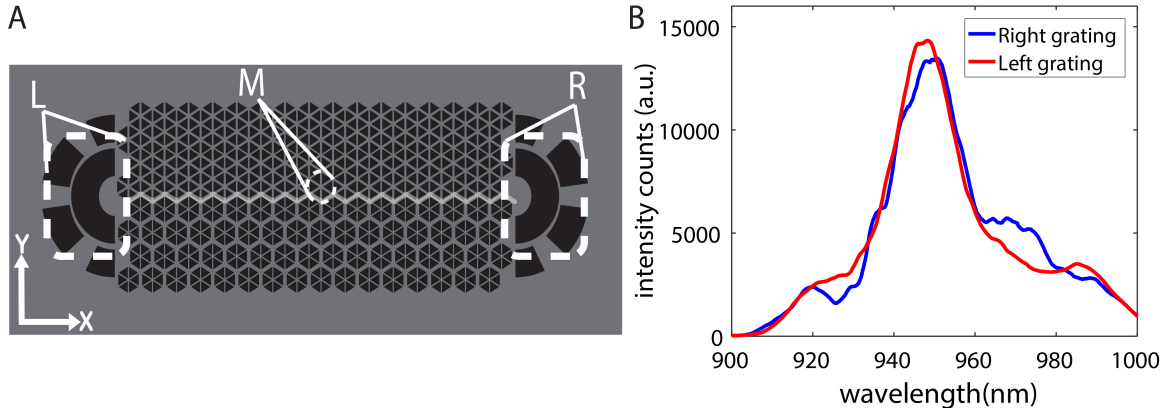


Figure B.2: Transmission data from left and right gratings. (A) Scheme for excitation and collection. (B) Transmitted signal collected from two gratings.

the gratings with almost overlapping transmission spectrum. Additionally, the area under the curves give approximately 40 million counts/sec for the gratings thus indicating equal coupling efficiency.

B.4 Coupling Efficiency

The coupling efficiency of emission from a single quantum emitter into the topological waveguide is defined by

$$\beta = \frac{I_L + I_R}{I_L + I_R + I_M} \quad (\text{B.1})$$

where I_L and I_R are the integrated photon counts propagating to the left and right waveguide modes respectively, and I_M is the photon counts emitted directly from the middle of the device into free space. We can estimate these intensities by measuring the brightness at the three locations denoted in the main text. Table B.1 shows the coupling efficiencies calculated for different dots coupled to our topological

device. The table reports integrated count rates for an integration time of 1s at each point. We determine the average to be 68%.

Coupled QDs	I_M	I_L	I_R	$\beta(\%)$
1	699	772	740	77.98
2	655	755	735	88.89
3	680	780	780	84.93
4	1300	1400	1900	75.23
5	802	1080	933	81.17
6	739	1021	654	78.85
7	795	1206	645	77.95
8	1090	1061	724	53.50
9	976	934	667	50.00
10	677	1079	807	92.44
11	869	728	819	54.90
12	1531	809	986	37.56
13	884	716	700	39.06
			Avg	68.65

Table B.1: Estimation of coupling efficiency.

Appendix C:

C.1 The polarization profile of a topological resonator

The electric field for the topological resonator mode is composed of two circularly-polarized components, where the high-field intensity points appear in different locations, as shown in Fig. C.1. Although these waveguides exhibit polarization-momentum locking, these plots indicate that the polarization profile changes in the transverse direction. If an emitter is located at the peak of right-circularly polarized light, and the QD is prepared to emit into right/left-circularly polarized light, then the emitted light travels in a clockwise/anti-clockwise fashion around the resonator.

C.2 Sample fabrication

The initial wafer is composed of 160 nm GaAs membrane with quantum dots grown at the center of the growth axis. 1 μm sacrificial layer of $\text{Al}_{0.8}\text{Ga}_{0.2}\text{As}$ beneath the active layer is used to undercut and to create suspended structures. The quantum dot density was $50 \mu\text{m}^{-2}$, which is high enough to find emitters resonant with the cavity mode. Based on the given quantum dot density and inhomogeneous broadening, the photon emitted by one quantum dot to be scattered by a second

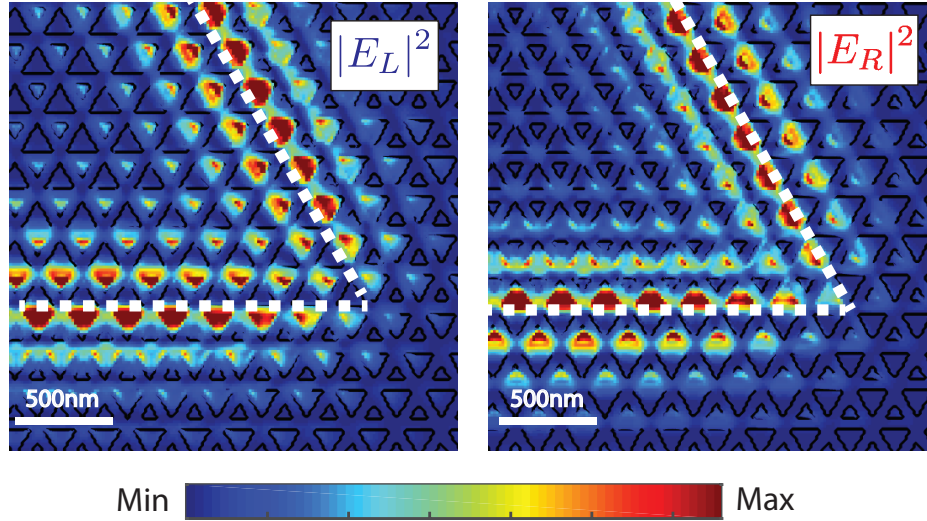


Figure C.1: Simulated left/right circular polarization components of the electric field. White dotted line marks the perimeter of the resonator.

is calculated to be extremely unlikely. Samples are first spin-coated with ZEP520A positive e-beam resist, followed by patterning using 100 keV high-resolution e-beam system. Exposed regions are developed by using ZED50 developer. After patterning, chlorine-based directional ICP etching is performed to transfer the patterns from ZEP520A hard mask to the GaAs layer. Lastly, selective wet etching using HF acid is performed to create a suspended structure with air on top and bottom.

Due to imperfections in e-beam exposure and directional dry etching, fabrication of small and sharp corners is challenging. The loss in the resolution is mitigated by using a modified layout design for triangles. We incorporate rectangular structures in the periphery in order to facilitate a homogeneous undercut of the sacrificial layer. Also, we fabricated an array of devices with different e-beam doses.

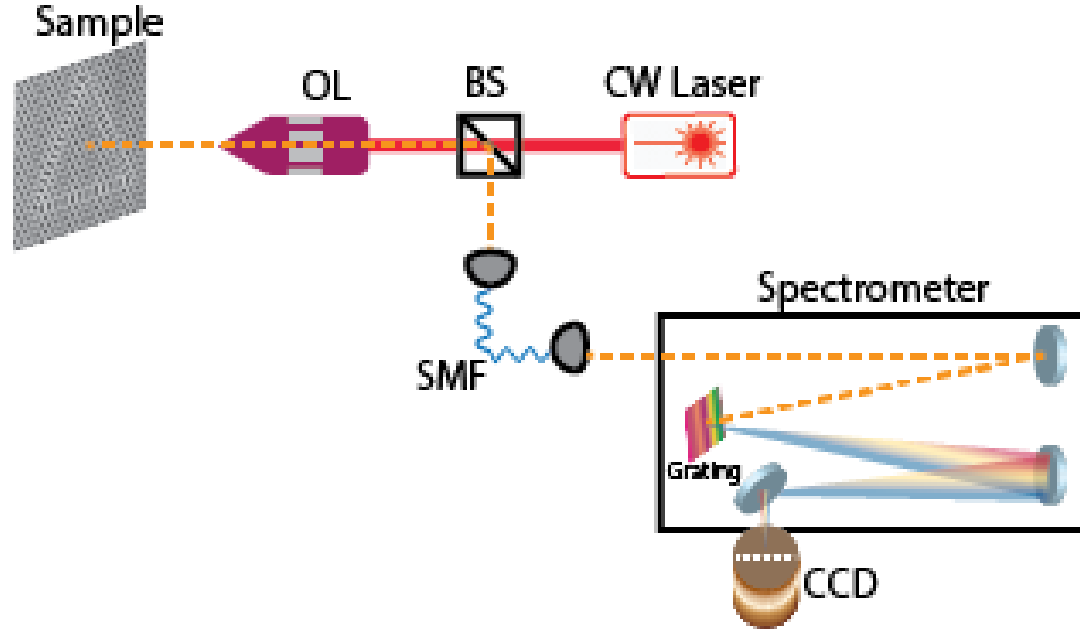


Figure C.2: Schematic of the experimental setup. OL, BS, SMF represent objective lens, beam splitter, single mode fiber, respectively.

C.3 Measurements

For photoluminescence measurement, we mount the sample on the cold finger of a cryostat (Attocube-Attodry system) which can be cooled down to a temperature 3K. The cold mount is surrounded by a superconducting magnet, which provided a variable magnetic field ranging from zero to 6 Tesla. In our setup, the sample is mounted in a Faraday configuration, i.e., the applied magnetic field is perpendicular to the sample plane.

We use a confocal microscope setup (Fig. C.2) for both exciting QDs and also collecting the photoluminescence (PL) signal from them. We use a continuous-wave 780nm diode laser for excitation. In the experiment, the collimated laser beam is focused on the sample by an objective lens with $NA=0.8$. We also image the

whole sample surface by shining a broadband light. This helps us to locate both the excitation and collection spots on the sample. The collected light is then focused on a single mode fiber (SMF) which acts as a spatial filter. For spectrally resolving individual QD lines, we pass this collected light through a spectrograph fitted with grating. In our case the spectral resolution is 0.02nm. This resolved light is then focused onto a nitrogen-cooled charge-coupled device (CCD) camera array capable of imaging at the single-photon level.

In experiment, due to $0.6 \mu m^2$ spot size of the laser spot, we excite roughly 25 quantum dots at the same time. Now owing to their inhomogeneous broadening and random placement all over the structure, they emit at different wavelengths and couple differently into the waveguide mode. We then isolate individual dots by spectrally filtering them through a grating spectrometer. We then confirm their coupling into the waveguide by spectrally locating them from emissions from different places of the device e.g. either from different locations on the resonator, or gratings at the end of the waveguide.

C.4 The quality factor of resonator in hybrid structures

We simulated the coupled waveguide-resonator system for different system parameters. In particular, we look at the behavior of resonator quality factor (Q) as we vary the amount of coupling between the waveguide and the resonator. Since we fix the perimeter of the resonator, the coupling strength only depends on the distance between the side of the resonator (facing the waveguide) and the topological

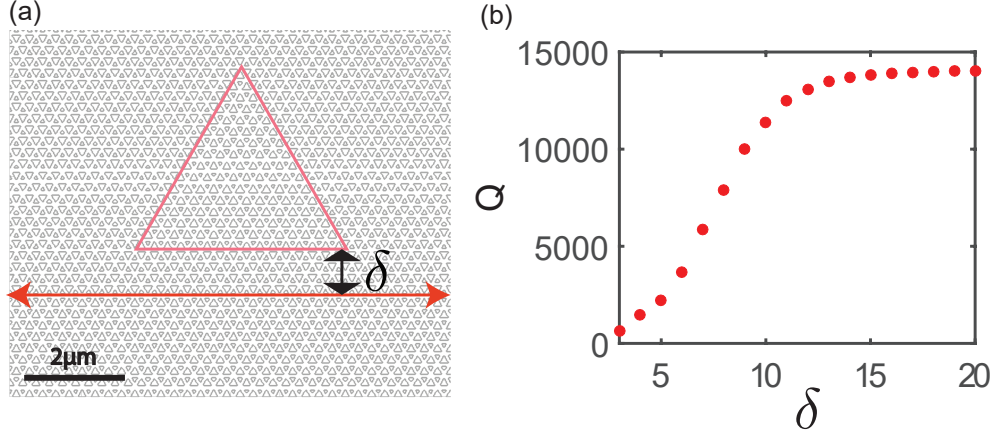


Figure C.3: Quality factor of cavity in hybrid structure : (a)Schematic of the simulation setup. Red super triangle indicates the resonator perimeter. The double arrowed red line indicates the position of the waveguide. (b) The quality factor (Q) versus distance (δ), showing saturation of Q at high values of δ

waveguide. We define the parameter δ as the number of unit cells, characterizing this coupling distance (Fig. C.3(a)). As shown in Fig. C.3(b) the Q of the resonator attains a saturation after δ . In other words, at this parameter, the resonator is weakly coupled into the waveguide. Also depending on the different values of δ one can create resonators of different Q. In our experiment, we choose δ to be 6.

C.5 Resonator designs with Valley-Hall physics

Apart from a triangular geometry, one can also fabricate other types of resonator designs with the valley-hall topological photonic crystal. Since these valley edge modes are immune to 60° and 120° , one can think of other resonator designs such as hexagon, rhombus, 3-side equal trapezoid, or more complicated designs, such

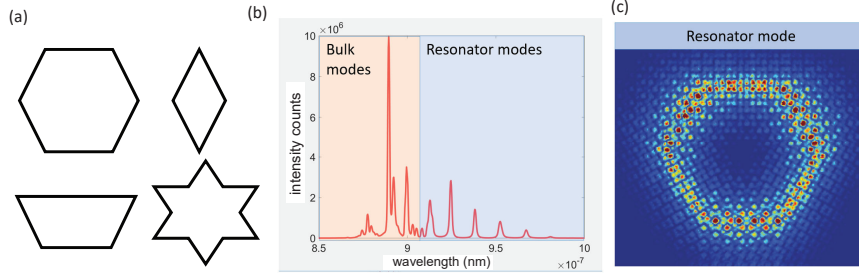


Figure C.4: More resonator ideas : (a) Possible resonator shapes using valley-Hall edge states (b) Simulated longitudinal modes of a hexagonal resonator showing both bulk modes and resonating modes. (c) The in-plane electric field distribution for one of the resonator modes.

as a hexagram (Fig. C.4 a).

Here we analyze a hexagonal resonator. As in the case of the triangular resonator in the main text, here the inside region of the hexagon is topologically distinct from the outside zone. Fig. C.4(b) shows the simulated modes in such a system. Color shaded regions correspond to different regimes on the band structure. Specifically, the orange shade represents the bulk modes in the system which are susceptible to disorder thus can provide random localized modes. And the blue band corresponds to edge band of the band structure. Thus these modes show strong confinement along the perimeter of the resonator (Fig. C.4(c)).

Bibliography

- [1] M. Z. Hasan and C. L. Kane, Colloquium: Topological insulators, *Rev. Mod. Phys.* **82**, 3045 (2010).
- [2] X.-L. Qi and S.-C. Zhang, Topological insulators and superconductors, *Rev. Mod. Phys.* **83**, 1057 (2011).
- [3] L. Lu *et al.*, Experimental observation of Weyl points, *Science* **349**, 622 (2015).
- [4] T. Ozawa, H. M. Price, A. Amo, N. Goldman, M. Hafezi, L. Lu, M. C. Rechtsman, D. Schuster, J. Simon, O. Zilberberg, and I. Carusotto, Topological photonics, *Rev. Mod. Phys.* **91**, 015006 (2019).
- [5] Z. Wang, Y. Chong, J. D. Joannopoulos, and M. Soljačić, Observation of unidirectional backscattering-immune topological electromagnetic states, *Nature* **461**, 772 (2009).
- [6] W.-J. Chen *et al.*, Experimental realization of photonic topological insulator in a uniaxial metacrystal waveguide, *Nat. Commun.* **5**, 5782 (2014).
- [7] W. Hu *et al.*, Measurement of a Topological Edge Invariant in a Microwave Network, *Phys. Rev. X* **5**, 011012 (2015).
- [8] S. A. Skirlo *et al.*, Experimental Observation of Large Chern Numbers in Photonic Crystals, *Phys. Rev. Lett.* **115**, 253901 (2015).
- [9] M. Hafezi, S. Mittal, J. Fan, A. Migdall, and J. M. Taylor, Imaging topological edge states in silicon photonics, *Nature Photon.* **7**, 1001 (2013).
- [10] S. Mittal *et al.*, Topologically Robust Transport of Photons in a Synthetic Gauge Field, *Phys. Rev. Lett.* **113**, 087403 (2014).

- [11] M. C. Rechtsman *et al.*, Photonic Floquet topological insulators, *Nature* **496**, 196 (2013).
- [12] M. C. Rechtsman *et al.*, Topological Creation and Destruction of Edge States in Photonic Graphene, *Phys. Rev. Lett.* **111**, 103901 (2013).
- [13] R. Kirchain and L. Kimerling, A roadmap for nanophotonics, *Nature Photon.* **1**, 303 (2007).
- [14] A. Jenkin, The road to nanophotonics, *Nature Photon.* **2**, 258 (2008).
- [15] E. Kuramochi *et al.*, Large-scale integration of wavelength-addressable all-optical memories on a photonic crystal chip, *Nature Photon.* **8**, 474 (2014).
- [16] J. L. O'Brien, A. Furusawa, and J. Vučković, Photonic quantum technologies, *Nature Photon.* **3**, 687 (2009).
- [17] J. Kimble, The quantum internet, *Nature* **453**, 1023 (2008).
- [18] A. Aspuru-Guzik and P. Walther, Photonic quantum simulators, *Nature Phys.* **8**, 285 (2012).
- [19] D. L. Underwood, W. E. Shanks, J. Koch, and A. A. Houck, Low-disorder microwave cavity lattices for quantum simulation with photons, *Phys. Rev. A* **86**, 023837 (2012).
- [20] M. Hafezi, M. D. Lukin, and J. M. Taylor, Non-equilibrium fractional quantum Hall state of light, *New J. Phys.* **15**, 063001 (2013).
- [21] A. Imamoglu, H. Schmidt, G. Woods, and M. Deutsch, Strongly Interacting Photons in a Nonlinear Cavity, *Phys. Rev. Lett.* **79**, 1467 (1997).
- [22] J. Klaers, J. Schmitt, F. Vewinger, and M. Weitz, Bose-Einstein condensation of photons in an optical microcavity, *Nature* **468**, 545 (2010).
- [23] K. M. Birnbaum *et al.*, Photon blockade in an optical cavity with one trapped atom, *Nature* **436**, 87 (2005).
- [24] B. Dayan *et al.*, A Photon Turnstile Dynamically Regulated by One Atom, *Science* **319**, 1062 (2008).
- [25] T. Peyronel *et al.*, Quantum nonlinear optics with single photons enabled by strongly interacting atoms, *Nature* **488**, 57 (2012).

- [26] P. Michler *et al.*, A Quantum Dot Single-Photon Turnstile Device, *Science* **290**, 2282 (2000).
- [27] D. Englund *et al.*, Controlling cavity reflectivity with a single quantum dot, *Nature* **450**, 857 (2007).
- [28] A. Reinhard *et al.*, Strongly correlated photons on a chip, *Nature Photon.* **6**, 93 (2012).
- [29] L.-H. Wu and X. Hu, Scheme for Achieving a Topological Photonic Crystal by Using Dielectric Material, *Phys. Rev. Lett.* **114**, 223901 (2015).
- [30] T. Ma, A. B. Khanikaev, S. H. Mousavi, and G. Shvets, Guiding Electromagnetic Waves around Sharp Corners: Topologically Protected Photonic Transport in Metawaveguides, *Phys. Rev. Lett.* **114**, 127401 (2015).
- [31] T. Ma and G. Shvets, All-Si valley-Hall photonic topological insulator, *New J. Phys.*, **18** p. 025012 (2016)
- [32] F. D. M. Haldane and S. Raghu, Possible Realization of Directional Optical Waveguides in Photonic Crystals with Broken Time-Reversal Symmetry, *Phys. Rev. Lett.* **100**, 013904 (2008).
- [33] T. Ochiai, Topological properties of bulk and edge states in honeycomb lattice photonic crystals: the case of TE polarization, *J. Phys.: Condens. Matter* **22**, 225502 (2010).
- [34] K. Fang, Z. Yu, and S. Fan, Realizing effective magnetic field for photons by controlling the phase of dynamic modulation, *Nature Photon.* **6**, 782 (2012).
- [35] M. Polini, F. Guinea, M. Lewenstein, H. C. Manoharan, and V. Pellegrini, Artificial honeycomb lattices for electrons, atoms and photons, *Nature Nanotech.* **8**, 625 (2013).
- [36] J. Petersen, J. Volz, A. Rauschenbeutel, Chiral nanophotonic waveguide interface based on spin-orbit interaction of light, *Science* **346**, 67 (2014).
- [37] I. Söllner *et al.*, Deterministic photon-emitter coupling in chiral photonic circuits, *Nature Nanotech.* **10**, 775 (2015).
- [38] R. J. Coles *et al.*, Chirality of nanophotonic waveguide with embedded quantum emitter for unidirectional spin transfer, *Nat Commun* **7**, 11183 (2016).

- [39] S. Y. Lin *et al.*, A three-dimensional photonic crystal operating at infrared wavelengths, *Nature* **394**, 251 (1998).
- [40] A. Blanco *et al.*, Large-scale synthesis of a silicon photonic crystal with a complete three-dimensional bandgap near 1.5 micrometres, *Nature* **405**, 437 (2000).
- [41] Y. Akahane, T. Asano, B.-S. Song, and S. Noda, High-Q photonic nanocavity in a two-dimensional photonic crystal, *Nature* **425**, 944 (2003).
- [42] T. Yoshie *et al.*, Vacuum Rabi splitting with a single quantum dot in a photonic crystal nanocavity, *Nature* **432**, 200 (2004).
- [43] S. G. Johnson, S. Fan, P. R. Villeneuve, J. D. Joannopoulos, and L. A. Kolodziejski, Guided modes in photonic crystal slabs, *Phys. Rev. B* **60**, 5751 (1999).
- [44] Y. A. Vlasov, M. O’Boyle, H. F. Hamann, and S. J. McNab, Active control of slow light on a chip with photonic crystal waveguides, *Nature* **438**, 65 (2005).
- [45] K. Hennessy *et al.*, Quantum nature of a strongly coupled single quantum dot–cavity system, *Nature* **445**, 896 (2007).
- [46] H. Kim, R. Bose, T. C. Shen, G. S. Solomon, and E. Waks, A quantum logic gate between a solid-state quantum bit and a photon, *Nature Photon.* **7**, 373 (2013).
- [47] P. Lodahl, S. Mahmoodian, and S. Stobbe, Interfacing single photons and single quantum dots with photonic nanostructures, *Rev. Mod. Phys.* **87**, 347 (2015).
- [48] C.-L. Hung, S. M. Meenehan, D. E. Chang, O. Painter, and H. J. Kimble, Trapped atoms in one-dimensional photonic crystals, *New J. Phys.* **15**, 083026 (2013).
- [49] A. Goban *et al.*, Atom–light interactions in photonic crystals, *Nat. Commun.* **5**, 4808 (2013).
- [50] A. González-Tudela, C.-L. Hung, D. E. Chang, J. I. Cirac, and H. J. Kimble, Subwavelength vacuum lattices and atom–atom interactions in two-dimensional photonic crystals, *Nature Photon.* **9**, 320 (2015).
- [51] J. S. Douglas *et al.*, Quantum many-body models with cold atoms coupled to photonic crystals, *Nature Photon.* **9**, 326 (2015).

- [52] V. Galitski and I. B. Spielman, Spin-orbit coupling in quantum gases, *Nature* **494**, 49 (2013).
- [53] G. Jotzu *et al.*, Experimental realization of the topological Haldane model with ultracold fermions, *Nature* **515**, 237 (2014).
- [54] Z. Yang *et al.*, Topological Acoustics, *Phys. Rev. Lett.* **114**, 114301 (2015).
- [55] V. Peano, C. Brendel, M. Schmidt, and F. Marquardt, Topological Phases of Sound and Light, *Phys. Rev. X* **5**, 031011 (2015).
- [56] P. Wang, L. Lu, and K. Bertoldi, Topological Phononic Crystals with One-Way Elastic Edge Waves, *Phys. Rev. Lett.* **115**, 104302 (2015)
- [57] R. Süsstrunk and S. D. Huber, Observation of phononic helical edge states in a mechanical topological insulator, *Science* **349**, 47 (2015).
- [58] L. Lu, J. D. Joannopoulos, and M. Soljačić, Topological photonics, *Nature Photon.* **8**, 821 (2014).
- [59] M. Hafezi and J. M. Taylor, Topological physics with light, *Physics Today* **67**, 68 (2014).
- [60] Z. Wang, Y. Chong, J. D. Joannopoulos, and M. Soljačić, Observation of unidirectional backscattering-immune topological electromagnetic states, *Nature* **461**, 772 (2009).
- [61] X. Cheng, C. Jouvaud, X. Ni, S. H. Mousavi, A. Z. Genack, and A. B. Khanikaev, Robust reconfigurable electromagnetic pathways within a photonic topological insulator, *Nat. Mater.* **15**, 542 (2016).
- [62] S. Mittal, S. Ganeshan, J. Fan, A. Vaezi and M. Hafezi, Measurement of topological invariants in a 2D photonic system, *Nature Photon.* **10**, 180 (2016).
- [63] M. Ringel, M. Pletyukhov and V. Gritsev, Topologically protected strongly correlated states of photons, *New J. Phys.* **16**, 113030 (2014).
- [64] H. Pichler, T. Ramos, A. J. Daley, and P. Zoller, Quantum optics of chiral spin networks, *Phys. Rev. A* **91**, 042116 (2015).
- [65] J. Cho, D. G. Angelakis, and S. Bose, Fractional Quantum Hall State in Coupled Cavities, *Phys. Rev. Lett.* **101**, 246809 (2008).

- [66] R. O. Umucallar and I. Carusotto, Fractional Quantum Hall States of Photons in an Array of Dissipative Coupled Cavities, *Phys. Rev. Lett.* **108**, 206809 (2012).
- [67] J. D. Joannopoulos, S. G. Johnson, J. N. Winn, R. D. Meade, *Photonic Crystals: Molding the Flow of Light*, (Princeton University Press, Princeton, NJ, 2008).
- [68] A. F. Koenderink, A. Alù, and A. Polman, Nanophotonics: Shrinking light-based technology, *Science* **348**, 516 (2015).
- [69] P. Lodahl, S. Mahmoodian, and S. Stobbe, Interfacing single photons and single quantum dots with photonic nanostructures, *Rev. Mod. Phys.* **87**, 347 (2015).
- [70] X.-D. Chen and J.-W. Dong, Valley-contrasting physics in all-dielectric photonic crystals: Orbital angular momentum and topological propagation, *Phys. Rev. B* **96**, 020202(2017).
- [71] A. H. Castro Neto, F. Guinea, N. M. R. Peres, K. S. Novoselov, and A. K. Geim, The electronic properties of graphene, *Rev. Mod. Phys.* **81**, 109 (2009).
- [72] K. Sakoda, *Optical Properties of Photonic Crystals*, (Springer-Verlag, Berlin, Germany, 2001).
- [73] E. D. Palik, *Handbook of Optical Constants of Solids I-III*, (Academic Press, San Diego, CA, 1997).
- [74] O. Painter *et al.*, Two-Dimensional Photonic Band-Gap Defect Mode Laser, *Science* **284**, 1819 (1999).
- [75] D. Englund *et al.*, Controlling the Spontaneous Emission Rate of Single Quantum Dots in a Two-Dimensional Photonic Crystal, *Phys. Rev. Lett.* **95**, 013904 (2005).
- [76] S. G. Johnson, S. Fan, P. R. Villeneuve, J. D. Joannopoulos, and L. A. Kolodziejski, Guided modes in photonic crystal slabs, *Phys. Rev. B* **60**, 5751 (1999).
- [77] B. A. Bernevig, T. L. Hughes, and S.-C. Zhang, Quantum Spin Hall Effect and Topological Phase Transition in HgTe Quantum Wells, *Science* **314**, 1757 (2006).

- [78] L. Xu, H. Wang, Y. D. Xu, H. Y. Chen, and J.-H. Jiang, Accidental degeneracy in photonic bands and topological phase transitions in two-dimensional core-shell dielectric photonic crystals, *Opt. Express* **24**, 18059-18071 (2016).
- [79] V. V. Albert, L. I. Glazman, and L. Jiang Topological Properties of Linear Circuit Lattices, *Phys. Rev. Lett.* **114**, 173902 (2015).
- [80] F. Xia, H. Wang, D. Xiao, M. Dubey, and A. Ramasubramaniam, Two-dimensional material nanophotonics, *Nature Photon.* **8**, 899 (2014).
- [81] I Aharonovich *et al.*, Diamond-based single-photon emitters, *Rep. Prog. Phys.* **74**, 076501 (2011).
- [82] I. Aharonovich, A. D. Greentree, and S. Prawer, Diamond photonics, *Nature Photon.* **5**, 397 (2011).
- [83] J. Dalibard, F. Gerbier, G. Juzeliūnas, P. Öhberg, Colloquium: Artificial gauge potentials for neutral atoms. *Rev. Mod. Phys.* **83**, 1523 (2011).
- [84] Eckardt, Colloquium: Atomic quantum gases in periodically driven optical lattices. *Rev. Mod. Phys.* **89**, 011004 (2017).
- [85] M. Hafezi, J. M. Taylor, Topological physics with light. *Physics Today* **67**, 68–69 (2014).
- [86] L. Kane, T. C. Lubensky, Topological boundary modes in isostatic lattices. *Nature Physics* **10**, 39–45 (2014).
- [87] J. Paulose, B.G.G. Chen, V. Vitelli, Topological modes bound to dislocations in mechanical metamaterials. *Nature Physics* **11**, 153–156 (2015).
- [88] R. Süsstrunk, S. D. Huber, Observation of phononic helical edge states in a mechanical topological insulator. *Science* **349**, 6243, 47-50 (2015).
- [89] X. Cheng, C. Jouvaud, X. Ni, S. H. Mousavi, A.Z. Genack, A. B. Khanikaev, Robust reconfigurable electromagnetic pathways within a photonic topological insulator. *Nature Materials* **15**, 542–548 (2016).
- [90] M. Hafezi, S. Mittal, J. Fan, A. Migdall, and J. M. Taylor, Imaging topological edge states in silicon photonics. *Nat. Photonics* **7**, 1001 (2013).
- [91] M. C. Rechtsman *et al.*, Photonic Floquet topological insulators. *Nature* **496**, 196–200 (2013).

- [92] M. Hafezi, E. A. Demler, M. D. Lukin, J. M. Taylor, Robust optical delay lines with topological protection. *Nature Physics* 7, 907–912 (2011).
- [93] L. Pilozzi, C. Conti, Topological lasing in resonant photonic structures. *Phys. Rev. B* 93, 195317 (2016).
- [94] G. Harari et al., Topological Lasers. Conference on Lasers and Electro-Optics, OSA Tech. Digest (online) (Opt. Soc. of Am., 2016).
- [95] P. St-Jean et al., Lasing in topological edge states of a one-dimensional lattice. *Nature Photonics* 11, 651-656 (2017).
- [96] P. Lodahl, S. Mahmoodian, S. Stobbe, A. Rauschenbeutel, P. Schneeweiss, J. Volz, H. Pichler, and P. Zoller, *Nature (London)* 541, 473 (2017).
- [97] I. Carusotto, C. Ciuti, Quantum fluids of light. *Rev. Mod. Phys.* 85, 299 (2013).
- [98] J. I. Cirac, H. J. Kimble, Quantum optics, what next? *Nature Photonics* 11, 18–20 (2017).
- [99] D.G. Angelakis, Ed., *Quantum Simulations with Photons and Polaritons* (Springer International Publishing, 2017).
- [100] S. Barik, H. Miyake, W. DeGottardi, E. Waks, M. Hafezi, Two-dimensionally confined topological edge states in photonic crystal. *New Journal of Physics* 18, 113013 (2016).
- [101] M. Bayer, G. Ortner, O. Stern, A. Kuther, A. A. Gorbunov, A. Forchel, P. Hawrylak, S. Fafard, K. Hinzer, T. L. Reinecke, S. N. Walck, J. P. Reithmaier, F. Klopff, and F. Schäfer, Fine structure of neutral and charged excitons in self-assembled In(Ga)As/(Al)GaAs quantum dots. *Phys. Rev. B* 65, 195315 (2002).
- [102] J. Petersen, J. Volz, and A. Rauschenbeutel, Chiral nanophotonic waveguide interface based on spin-orbit interaction of light, *Science* 346, 67 (2014).
- [103] T. Kariyado, X. Hu, Topological States Characterized by Mirror Winding Numbers in Graphene with Bond Modulation. *Scientific Reports* 7, 16515 (2017).
- [104] H. Pichler, T. Ramos, A. J. Daley, P. Zoller, Quantum optics of chiral spin networks. *Phys. Rev. A* 91, 042116 (2014).

- [105] M. Ringel, M. Pletyukhov, V. Gritsev, Topologically protected strongly correlated states of photons. *New Journal of Physics* 16, 113030 (2014).
- [106] A. Metelmann, A. A. Clerk, Nonreciprocal Photon Transmission and Amplification via Reservoir Engineering. *Phys. Rev. X* 5, 021025 (2015).
- [107] R. O. Umucalilar and I. Carusotto, Fractional Quantum Hall States of Photons in an Array of Dissipative Coupled Cavities. *Phys. Rev. Lett.* 108, 206809 (2012).
- [108] M. Hafezi, M. D. Lukin, and J. M. Taylor, Non-equilibrium fractional quantum Hall state of light. *New J. Phys.* 15, 063001 (2013).
- [109] H. Pichler, T. Ramos, A. J. Daley, and P. Zoller, Quantum optics of chiral spin networks, *Phys. Rev. A* 91, 042116 (2015).
- [110] H. Pichler, S. Choi, P. Zoller, and M. D. Lukin, Universal photonic quantum computation via time-delayed feedback, *Proc. Natl. Acad. Sci. USA* 114, 11362 (2017).
- [111] I. Shomroni, S. Rosenblum, Y. Lovsky, O. Bechler, G. Guendelman, and B. Dayan, All-optical routing of single photons by a one-atom switch controlled by a single photon, *Science* 345, 903 (2014).
- [112] C. Junge, D. O’Shea, J. Volz, and A. Rauschenbeutel, Strong Coupling between Single Atoms and Nontransversal Photons, *Phys. Rev. Lett.* 110, 213604 (2013).
- [113] S. J. M. Habraken, K. Stannigel, M. D. Lukin, P. Zoller, and P. Rabl, Continuous mode cooling and phonon routers for phononic quantum networks, *New J. Phys.* 14, 115004 (2012).
- [114] V. Peano, C. Brendel, M. Schmidt, and F. Marquardt, Topological Phases of Sound and Light, *Phys. Rev. X* 5, 031011 (2015).
- [115] B. Vermersch, P.-O. Guimond, H. Pichler, and P. Zoller, Quantum State Transfer via Noisy Photonic and Phononic Waveguides, *Phys. Rev. Lett.* 118, 133601 (2017).
- [116] G. Calajó, M. J. A. Schuetz, H. Pichler, M. D. Lukin, P. Schneeweiss, J. Volz, and P. Rabl, Quantum acousto-optic control of light-matter interactions in nanophotonic networks, *Phys. Rev. A* 99, 053852 (2019).

- [117] I. Söllner, S. Mahmoodian, S. L. Hansen, L. Midolo, A. Javadi, G. Kiršanskė, T. Pregnolato, H. El-Ella, E. H. Lee, J. D. Song, S. Stobbe, and P. Lodahl, Deterministic photon–emitter coupling in chiral photonic circuits, *Nat. Nanotechnol.* 10, 775 (2015).
- [118] R. J. Coles, D. M. Price, J. E. Dixon, B. Royall, E. Clarke, P. Kok, M. S. Skolnick, A. M. Fox, and M. N. Makhonin, Chirality of nanophotonic waveguide with embedded quantum emitter for unidirectional spin transfer, *Nat. Commun.* 7, 11183 (2016).
- [119] Z. Wang, Y. Chong, J. D. Joannopoulos, and M. Soljacić, Observation of unidirectional backscattering-immune topological electromagnetic states, *Nature (London)* 461, 772 (2009).
- [120] M. Hafezi, E. A. Demler, M. D. Lukin, and J. M. Taylor, Robust optical delay lines with topological protection, *Nat. Phys.* 7, 907 (2011).
- [121] M. C. Rechtsman, J. M. Zeuner, Y. Plotnik, Y. Lumer, D. Podolsky, F. Dreisow, S. Nolte, M. Segev, and A. Szameit, Photonic Floquet topological insulators, *Nature (London)* 496, 196 (2013).
- [122] S. Mittal, J. Fan, S. Faez, A. Migdall, J. M. Taylor, and M. Hafezi, Imaging topological edge states in silicon photonics, *Phys. Rev. Lett.* 113, 087403 (2014).
- [123] X. Cheng, C. Jouvaud, X. Ni, S. H. Mousavi, A. Z. Genack, and A. B. Khanikaev, Robust reconfigurable electromagnetic pathways within a photonic topological insulator, *Nat. Mater.* 15, 542 (2016).
- [124] B. Bahari, A. Ndao, F. Vallini, A. El Amili, Y. Fainman, and B. Kanté, Nonreciprocal lasing in topological cavities of arbitrary geometries, *Science* 358, 636 (2017).
- [125] M. A. Bandres, S. Wittek, G. Harari, M. Parto, J. Ren, M. Segev, D. N. Christodoulides, and M. Khajavikhan, Topological insulator laser: Experiments, *Science* 359, eaar4005 (2018).
- [126] J.-W. Dong, X.-D. Chen, H. Zhu, Y. Wang, and X. Zhang, Valley photonic crystals for control of spin and topology, *Nat. Mater.* 16, 298 (2017).
- [127] X.-D. Chen, F.-L. Zhao, M. Chen, and J.-W. Dong, Valley-contrasting physics in all-dielectric photonic crystals: Orbital angular momentum and topological propagation, *Phys. Rev. B* 96, 020202(R) (2017).

- [128] X.-T. He, E.-T. Liang, J.-J. Yuan, H.-Y. Qiu, X.-D. Chen, F.-L. Zhao, and J.-W. Dong, A silicon-on-insulator slab for topological valley transport, *Nat. Commun.* **10**, 872 (2019).
- [129] J. Noh, S. Huang, K. P. Chen, and M. C. Rechtsman, Observation of Photonic Topological Valley Hall Edge States, *Phys. Rev. Lett.* **120**, 063902 (2018).
- [130] M. I. Shalaev, W. Walasik, A. Tsukernik, Y. Xu, and N. M. Litchinitser, Robust topologically protected transport in photonic crystals at telecommunication wavelengths, *Nat. Nanotechnol.* **14**, 31 (2019).
- [131] T. Ma and G. Shvets, All-Si valley-Hall photonic topological insulator, *New J. Phys.* **18**, 025012 (2016).
- [132] A. Sipahigil, R. E. Evans, D. D. Sukachev, M. J. Burek, J. Borregaard, M. K. Bhaskar, C. T. Nguyen, J. L. Pacheco, H. A. Atikian, C. Meuwly, R. M. Camacho, F. Jelezko, E. Bielejec, H. Park, M. Lončar, and M. D. Lukin, An integrated diamond nanophotonics platform for quantum-optical networks, *Science* **354**, 847 (2016).
- [133] D. Bhatti, R. Schneider, S. Oettel, and J. von Zanthier, Directional Dicke Subradiance with Nonclassical and Classical Light Sources, *Phys. Rev. Lett.* **120**, 113603 (2018).
- [134] M. Bello, G. Platero, J. I. Cirac, and A. González-Tudela, Unconventional quantum optics in topological waveguide QED, *Sci. Adv.* **5**, eaaw0297 (2019).
- [135] J. Perczel, J. Borregaard, D. E. Chang, H. Pichler, S. F. Yelin, P. Zoller, and M. D. Lukin, Topological Quantum Optics in Two-Dimensional Atomic Arrays, *Phys. Rev. Lett.* **119**, 023603 (2017).
- [136] D. Press, T. D. Ladd, B. Zhang, and Y. Yamamoto, Complete quantum control of a single quantum dot spin using ultrafast optical pulses, *Nature* **456**, 218 (2008).
- [137] J. Berezovsky, M. H. Mikkelsen, N. G. Stoltz, L. A. Coldren, and D. D. Awschalom, Picosecond Coherent Optical Manipulation of a Single Electron Spin in a Quantum Dot, *Science* **320**, 349 (2008).
- [138] S. Sun, H. Kim, G. S. Solomon, and E. Waks, A quantum phase switch between a single solid-state spin and a photon. *Nature Nanotech* **11**, 539–544 (2016).

- [139] M. D. Birowosuto *et al.*, Fast Purcell-enhanced single photon source in 1,550-nm telecom band from a resonant quantum dot-cavity coupling, *Sci. Rep.* **2**, 321 (2012).
- [140] A. Srivastava *et al.*, *Nature Nanotech.* **10**, 491 (2015).
- [141] Y.-M. He *et al.*, *Nature Nanotech.* **10**, 497 (2015).
- [142] M. Koperski *et al.*, *Nature Nanotech.* **10**, 503 (2015).
- [143] M. W. McCutcheon and M. Lončar, *Opt. Express* **16**, 19136 (2008).
- [144] M. Eichenfield, R. Camacho, J. Chan, K. J. Vahala, and O. Painter, *Nature* **459**, 550 (2009).
- [145] I Aharonovich *et al.*, *Rep. Prog. Phys.* **74**, 076501 (2011).
- [146] I. Aharonovich, A. D. Greentree, and S. Prawer, *Nature Photon.* **5**, 397 (2011).
- [147] W. F. Koehl, B. B. Buckley, F. J. Heremans, G. Calusine, and D. D. Awschalom, *Nature* **479**, 84 (2011).
- [148] S. Castelletto *et al.*, *Nature Mater.* **13**, 151 (2014).
- [149] M. Widmann *et al.*, *Nature Mater.* **14**, 164 (2015).
- [150] D. Englund *et al.*, *Nano Lett.* **10**, 3922 (2010).
- [151] S. Yamada, B.-S. Song, T. Asano, and S. Noda, *Appl. Phys. Lett.* **99**, 201102 (2011).
- [152] J. Riedrich-Möller *et al.*, *Nature Nanotech.* **7**, 69 (2011).
- [153] A. Faraon, C. Santori, Z. Huang, V. M. Acosta, and R. G. Beausoleil, *Phys. Rev. Lett.* **109**, 033604 (2012).
- [154] J. D. Thompson *et al.*, *Science* **340**, 1202 (2013).
- [155] T. G. Tiecke *et al.*, *Nature (London)* **508**, 241 (2014).
- [156] C.-L. Hung, S. M. Meenehan, D. E. Chang, O. Painter, and H. J. Kimble, *New J. Phys.* **15**, 083026 (2013).

- [157] A. Goban *et al.*, Nat. Commun. **5**, 4808 (2013).
- [158] A. González-Tudela, C.-L. Hung, D. E. Chang, J. I. Cirac, and H. J. Kimble, Nature Photon. **9**, 320 (2015).
- [159] J. S. Douglas *et al.*, Nature Photon. **9**, 326 (2015).
- [160] L.-H. Wu and X. Hu, Sci. Rep. **6**, 24347 (2105).
- [161] K. Sakoda, *Optical Properties of Photonic Crystals*, (Springer-Verlag, Berlin, Germany, 2001).
- [162] D. N. Sheng, Z. Y. Weng, L. Sheng, and F. D. M. Haldane, Phys. Rev. Lett. **97**, 036808 (2006).
- [163] N. W. Ashcroft and N. D. Mermin, *Solid State Physics*, (Harcourt College Publishers, Fort Worth, 1976).
- [164] M. Z. Hasan and C. L. Kane, Rev. Mod. Phys. **82**, 3045 (2010).
- [165] R. Jackiw and C. Rebbi, Phys. Rev. D **13**, 3398 (1976).